

# Emergent topological phases in an extended Su-Schrieffer-Heeger model with Rashba spin-orbit interaction, higher order hopping and domain wall

Hemant Kumar Sharma,<sup>1,\*</sup> Arijit Saha,<sup>1,2,†</sup> and Saptarshi Mandal<sup>1,2,‡</sup>

<sup>1</sup>*Institute of Physics, Sachivalaya Marg, Bhubaneswar-751005, India*

<sup>2</sup>*Homi Bhabha National Institute, Training School Complex, Anushakti Nagar, Mumbai 400094, India*

(Dated: October 15, 2024)

We theoretically investigate emergent topological phases in an extended spin-full Su-Schrieffer-Heeger (SSH) model considering Rashba spin-orbit interaction, all possible complex next to next nearest neighbor (NNNN) hopping preserving Chiral symmetry. Our analysis finds exact condition for which the topological phases of both the spin sectors could be independently varied. We show that it necessarily depends on complex NNNN only. We elaborate in detail the emergent topological phases, its criteria through analytic determination of non-trivial gap-closing condition due to the presence of  $\cos 2k$  term. We also find that the profile of topological edge modes for finite winding numbers depend non-monotonously on the value of NNNN hopping elucidating competing effect of model parameters. We extend our study to few coupled chains and show explicitly that depending on the parameters all possible winding number ranging from zero to  $2N$  could be obtained, where  $N$  is the number of chains considered. Finally we incorporate the study of domain wall and remarkably we find that the location of mid-gap zero energy state by changing the values of model parameters. Our study could be of immensely useful for future applications in quantum technology.

## I. INTRODUCTION

Recent studies in condensed matter physics has found a strong interest on various topological aspects [1] of varieties of systems. Initially with the discovery of the quantum Hall effect [2, 3], it has now covered many features such as spin-orbit coupled topological band insulators [4–7], topological superconductors [7, 8], and other related topics that have all been immensely influenced by the development of understanding of topological band theory [9–12]. Present studies on topological insulators are examining the role of various effects such as disorder, dislocations [13–18], and effects of interactions [19–22] as well. In exploring topological aspect of condensed matter systems, few paradigmatic tight binding models such as Haldane model [23], one dimensional Kitaev model [24] and Su-Schrieffer-Heeger (SSH) model [25, 26] have contributed new understanding. There has been several proposals to experimentally realize Haldane model in relevant materials or in cold atomic system [27–30]. Realization of Majorana zero modes (MZM) in one dimensional Kitaev model has recently been materialized in coupled quantum dots [31, 32] and Rashba nano wire [33–35]. On the other hand, SSH model has been proposed mainly on mechanical or electrical circuits [36–41] along with recent proposals on atomic chains [42]. Recently there has been interesting proposals to realize Kitaev model as coupled SSH chains as well [43–46]. These pioneering models have been explored further by various extensions [47–58] of different kind to investigate new topological aspects with aims of pushing the theoretical knowledge as well as possibility of novel practical applications [59–62].

Such extensions appeared to be very useful and non-trivial to establish new topological phases. For example the Kane-Mele [47] model can be thought of as an extension of Haldane model [23] to spin-ful system. Further extension of Kane-Mele or Haldane model to include NNNN hopping [50–52] or staggered flux [48–50] yielded new topological phases. Another useful way to extend a model topological system in a given dimension is to consider many such stacked layers to build a new one in higher dimensions. These examples include bi-layer (and three dimensional) Haldane model [63–65], Kitaev models in higher dimensions and SSH model in higher-dimension [66–69]. SSH model being one of the oldest yet impactful model, went through many extensions and modifications [53–58]. For the simplest one dimensional case, effect of next nearest neighbor interaction which allows hopping between same sub-lattices has been considered [70]. Various other aspects such as effect of NNNN interactions [57, 71–73] and effect of modulations in hopping parameters [74] has been investigated to manipulate the topological phases parametrically. Recently the effects of impurities [75], long range hoppings [76], and spin-orbit interactions [77, 78] have been studied in the extended SSH model [79] with an aim either to examine the stability of topological phases or its dependence on extended parameter space. Furthermore the studies on coupled SSH chains [54–56, 80–85] has provided valuable insight to understand the emergent topological phases in higher dimensions such as two [66, 67] and three dimensions [68, 69].

In this paper we have re-visited the SSH model and investigated certain aspects of an extended version of it with an objective to find new topological phases and how to manipulate those. The extended SSH model considered here contains i) Rashba spin-orbit interaction (RSOI), ii) modified inter-cell hopping and all possible NNNN hopping on the SSH chain which connects in-

\* hemant.sharma@iopb.res.in

† arijit@iopb.res.in

‡ saptarshi@iopb.res.in

equivalent sub-lattices between ‘ $i$ ’th and ‘ $i \pm k$ ’ unit cell with  $k = 1, 2$ . We have shown that for such cases, the winding number can be manipulated from  $0 \rightarrow 1 \rightarrow 2$  for a single spinful SSH chain and find the criteria for these phases, mainly we show that there has to be certain relations between the imaginary part of hopping interactions which allows this. The winding number one indicates a case when only one spin sector is topological and other spin sector is non-topological. Next we consider coupling between few such extended SSH chains. By considering two and four such coupled chains we explicitly show that our scheme can generate topological phase characterized by arbitrary winding number marked by any integer from 0 to  $2\mathcal{N}$  where  $\mathcal{N}$  is the number of coupled chains considered. Finally we extend our study to include a domain wall potential [75] and investigate the role of various parameters. Remarkably we find that the position of zero energy mid gap state can be controlled by varying certain parameters. We also extend the domain wall study for coupled SSH chains and end with a discussion and outlook.

The structure of the paper is following. Sec. II deals with various aspects of extended SSH model as follows. We define the model explaining all the parameters in detail, discuss the spectrum and gap closing points at topological phase transitions in relevant parameter space in II A. In II B we discuss some general aspect of the extended SSH model such as parametric dependencies of topology and the general form of trajectory of  $\vec{h}(k)$  in  $k_x, k_y$  plane where  $h(\vec{k}) \cdot \vec{\sigma}$  denotes the effective Hamiltonian for a given spin. In II C we chart out the topological phase diagrams in relevant parameter spaces in detail and present the criteria and necessary condition for realizing these phases. Finally in II D, we discuss the topological edge modes obtained in different phases for an open chain and its parametric dependencies. In Sec III we consider two and four coupled SSH chains and present the study of its topological aspect briefly. In IV we study the effect of domain wall on this extended SSH model and the role of different parameters. We summarize and conclude our paper in V with possible future directions.

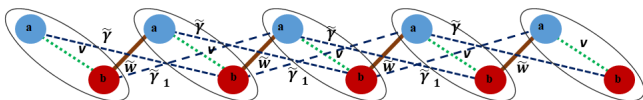


Figure 1. A cartoon of extended SSH model is shown.  $v$  and  $\tilde{w}$  denote the intra and interchain NN hopping whereas  $\tilde{\gamma}$  represents NNN hopping.  $\tilde{w}$  and  $\tilde{\gamma}$  are taken to be complex in general.

## II. EXTENDED SSH MODEL

### A. Model

The Hamiltonian for hybrid SSH model which we consider is given as follows,

$$H = \sum_{n=1}^N \left( v\psi_{n,a}^\dagger\psi_{n,b} + \tilde{w}\psi_{n+1,a}^\dagger\psi_{n,b} + h.c \right) + \left( i\alpha_{R1}\psi_{n,b}^\dagger\sigma_z\psi_{n,a} + i\alpha_{R2}\psi_{n+1,a}^\dagger\sigma_z\psi_{n,b} + h.c \right) + \left( \tilde{\gamma}\psi_{n,a}^\dagger\psi_{n+1,b} + \tilde{\gamma}_1\psi_{n,b}^\dagger\psi_{n+2,a} + h.c \right) \quad (1)$$

In the above  $\psi_{i,s}^\dagger = (c_{i,s,\uparrow}^\dagger, c_{i,s,\downarrow}^\dagger)$  with ‘ $s$ ’ denoting the sub-lattice indices ‘ $a$ ’ and ‘ $b$ ’ denoted by blue and red filled circles respectively in Fig.1. ‘ $v$ ’ and ‘ $\tilde{w}$ ’ denote the intracell and intercell nearest neighbor (NN) hopping respectively between the two sublattices and corresponds to the original SSH model. The second line refers to intracell and intercell Rashba spin-orbit interaction and in the spirit of SSH model we have considered different magnitude for intracell and intercell Rashba interaction represented by  $\alpha_{R1}$  and  $\alpha_{R2}$  respectively. The third line of the Eqn. 1 denotes a NNNN neighbor hopping and are denoted by  $\tilde{\gamma}$ ,  $\tilde{\gamma}_1$  as shown in Fig. 1 by black dashed line. For generalization we have assumed two types of hopping for two different type of NNNN hopping which covers either a  $v - w - v$  bonds or  $w - v - w$  bonds by  $\gamma_1$  and  $\gamma$  respectively. This has been shown in Fig.1 by dense and sparse dashed lines respectively. We note that as we consider the one dimensional SSH chain to be in  $x$ -direction, the generalized Rashba spin-orbit interaction  $ic_i(\vec{\sigma} \times \vec{d}_{ij})_z c_j$  does not causes any spin-flip process but only changes sign between the two spin-sectors[48, 49]. This effectively modifies the intracell and intercell nearest-neighbor hopping for two spin sectors differently. We have used  $\tilde{w}$  and  $\tilde{\gamma}$  (instead of  $w$  and  $\gamma$ ) which signifies that these hopping parameters could be complex in general. This complex hopping parameters play important role in the subsequent analysis. For future usage we decompose these parameters explicitly into real and imaginary part given as  $\tilde{w} = w + i\xi/2$  and  $\tilde{\gamma} = \gamma + i\eta/2$  and  $\tilde{\gamma}_1 = \gamma_1 + i\eta_1/2$  where  $w, \gamma, \xi, \eta, \eta_1$  are all real. After a straightforward Fourier transformation of the Hamiltonian  $H$  given in Eqn. 1 we can rewrite  $H$  as  $\Psi_k^\dagger \mathcal{H}(k) \Psi_k$  where  $\mathcal{H}(k)$  is given below.

$$\mathcal{H}(k) = \left( v + w_+ \cos k - \frac{\xi_-}{2} \sin k - \frac{\eta_1}{2} + \gamma_1 \cos 2k \right) \Gamma_1 - \left( w_- \sin k + \gamma_1 \sin 2k + \frac{\xi_+}{2} \cos k + \frac{\eta_1}{2} \cos 2k \right) \Gamma_2 + (\alpha_{R1} - \alpha_{R2} \cos k) \Gamma_3 - \alpha_{R2} \sin k \Gamma_4. \quad (2)$$

Where we have used  $w_\pm = (w \pm \gamma)$ ,  $\xi_\pm = \xi \pm \eta$ . In the above, various  $\Gamma$ ’s are  $4 \times 4$  matrices which are de-

finer terms of two dimensional Pauli matrices as follows,  $\Gamma_1 = \sigma_x \otimes \sigma_0$ ,  $\Gamma_2 = \sigma_y \otimes \sigma_0$ ,  $\Gamma_3 = \sigma_y \otimes \sigma_x$  and  $\Gamma_4 = \sigma_x \otimes \sigma_z$ . In Eq. 2 we have used the basis vector  $\Psi_k^\dagger = (c_{ka,\uparrow}^\dagger, c_{ka,\downarrow}^\dagger, c_{kb,\uparrow}^\dagger, c_{kb,\downarrow}^\dagger)$ . One can check easily that the Hamiltonian in Eq.(2) respects the Chiral symmetry ,  $S = \sigma_0 \otimes \sigma_z : S^{-1}\mathcal{H}(k)S = -\mathcal{H}(k)$ .

The presence of Rashba spin-orbit interaction in the

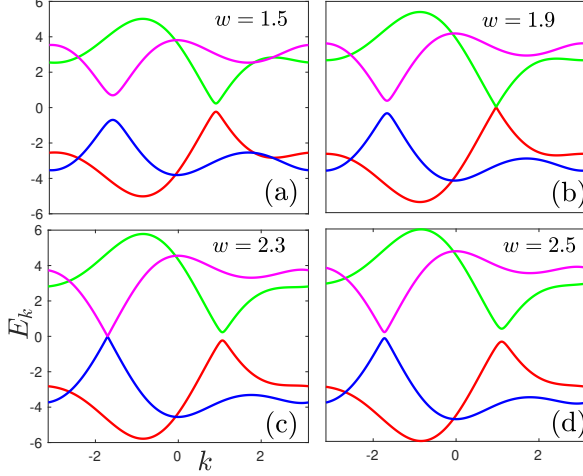


Figure 2. We plot the dispersion ( $E_k$ ) for various values of  $w$  as shown in each panel. In each plot values of other parameters are taken as  $v = 1, \alpha_{R1} = 2, \alpha_{R2} = 1, \gamma = 0.5, \eta = 2.5$ . The panel (a) corresponds both the spin-sectors being non-topological with winding number zero i.e  $W = 0$ . Panel (b) shows gap closing for up-spin sector and it becomes topological with  $W = 1$  for slight increment in  $w > 1.9$ . The Panel (c) depicts the gap closing for down spin-sector. As we increase  $w$  further, both the spin-sectors become gapped and topological as shown in panel (d).

one-dimensional SSH chain breaks the spin-degeneracies of the bands and as a result we obtain four non-degenerate bands, two of which are valence bands and rest are conduction bands. In Fig. 2 we plot these four bands for various set of parameters elucidating band gap closing and reopening near the topological phase transitions. As will be evident later that different gap-closing condition for each spin-sectors happen due to the complex NNNN hopping which allows two gap-closing points, one for each spin sectors and they occur at different ' $k$ ' points in general for each spin sectors. Thus it paves way to manipulate the topological nature of a given spin sector independently.

$$\mathcal{E}_{\uparrow,\pm}(k) = \pm|v_{\uparrow} + w_{\uparrow}e^{ik} + \tilde{\gamma}e^{-ik} + \tilde{\gamma}_1e^{i2k}|, \quad (3)$$

$$\mathcal{E}_{\downarrow,\pm}(k) = \pm|v_{\downarrow} + w_{\downarrow}e^{ik} + \tilde{\gamma}e^{-ik} + \tilde{\gamma}_1e^{i2k}|. \quad (4)$$

In the above  $v_{\uparrow} = v + i\alpha_{R1}$ ,  $w_{\uparrow} = \tilde{w} + i\alpha_{R2}$  and  $v_{\downarrow} = v - i\alpha_{R1}$ ,  $w_{\downarrow} = \tilde{w} - i\alpha_{R2}$ . Though the gap closing condition can be obtained with  $\mathcal{E}_{\sigma,\pm} = 0$  from Eqn. 4, it appears that due to  $\gamma$  term and associated ' $k$ ' dependency it does not yield a simple expression. To obtain the gap-closing condition we write the Hamiltonian in the ba-

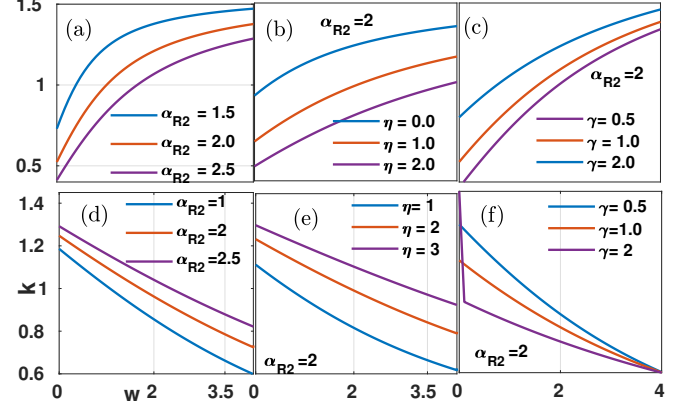


Figure 3. Gap closing momentum  $k$  is plotted against  $w$  for various combination of parameters. For all panel we have taken  $v = 1$ . In panel (a) various colors show fixed values of  $\alpha_{R2}$  with  $\eta = \eta_1 = 0, \gamma = \gamma_1 = 0$  while  $\alpha_{R1}$  is determined by self-consistent condition. In the panel (b) dependence on  $\eta$  is shown for a given  $\gamma, \alpha_{R2}$  with  $\alpha_{R2} = 2.0, \gamma = 0.5, \eta_1 = \gamma_1 = 0$ . In panel (c) we show the dependence on various values of  $\gamma$  with  $\eta = 2, \eta_1 = \gamma_1 = 0, \alpha_{R2} = 2$ . Here also  $\alpha_{R1}$  being determined by the normalization condition. The panel (d) corresponds various values of  $\alpha_{R2}$  with  $\eta = \eta_1 = 2, \gamma = \gamma_1 = 0.5$ . Panel (e) depicts the case with different values of  $\eta$  with fixed  $\gamma = \gamma_1 = 0.5, \eta = \eta_1 = 2$ . Finally panel (f) corresponds  $\eta = \eta_1 = 1, \gamma = \gamma_1, \alpha_{R2} = 2$ .

sis  $\Psi_k^\dagger = (c_{ka,\uparrow}^\dagger, c_{kb,\uparrow}^\dagger, c_{ka,\downarrow}^\dagger, c_{kb,\downarrow}^\dagger)$  such that for each spin sector Hamiltonian can be written as  $h_{k,\beta} = \sum_{\alpha} h_{\alpha,k}^k \sigma_{\alpha}$  where  $h_{\alpha,k}^k$  is given below.

$$h_{\uparrow(\downarrow),x}^k = v + (w + \gamma) \cos k - \left( \frac{\xi}{2} \pm \alpha_{R2} - \frac{\eta}{2} \right) \sin k + \gamma_1 \cos 2k - \frac{\eta_1}{2} \sin 2k \quad (5)$$

$$h_{\uparrow(\downarrow),y}^k = \mp \alpha_{R1} + \left( \frac{\xi}{2} \pm \alpha_{R2} + \frac{\eta}{2} \right) \cos k \mp (w - \gamma) \sin k + \gamma_1 \sin 2k + \frac{\eta_1}{2} \cos 2k \quad (6)$$

From the above equations we find that  $\xi$  and  $\eta$  appears together with  $\alpha_{R2}$ . Hence to simplify the parametric dependencies, we choose  $\eta = -\xi$  without loss of generality and changing the conclusion of subsequent analysis. In the above upper and lower sign correspond to up and down spin sector respectively. From the above set of equation we find that expressions for  $h_{\uparrow}^k$  and  $h_{\downarrow}^k$  are related by a change in sign in  $\alpha_{R1}$ ,  $\alpha_{R2}$  and  $\eta_1$ . In the appendix we give the details of solutions for  $h_{\sigma,x}^k = h_{\sigma,y}^k = 0$ . We notice that in the absence of  $\gamma_1$  and  $\eta_1$ , the above equations can be solved easily for  $\cos k$  and  $\sin k$  and the normalization condition  $\sin^2 k + \cos^2 k = 1$  gives the equation for the curve in  $h_x, h_y$  plane. Also one can easily solve for  $h_x = h_y = 0$  in this limit yielding the

gapless condition. In Fig. 3 we plot the ‘ $k$ ’ at the topological phase transition as a function of ‘ $w$ ’ for different sets of parameter. In Fig. 3, panel (a) corresponds to the simple case with  $\gamma = \gamma_1 = 0, \eta = \eta_1 = 0$  and finite  $\alpha_{R2}$ . Note that as  $w$  is varied, each point corresponds different value of  $\alpha_{R1}$  which is self-consistently determined from the normalization condition. Throughout our paper we have set  $v = 1$ . It is interesting to note that in the absence of  $\gamma_1$ , there is steady increment in the magnitude of gap-closing point as evident from panel (a),(b) and (c). On the other hand once we have finite  $\gamma_1$ , the magnitude of gap closing point steadily decreases as we increase  $w$ , see lower panels of Fig. 3.

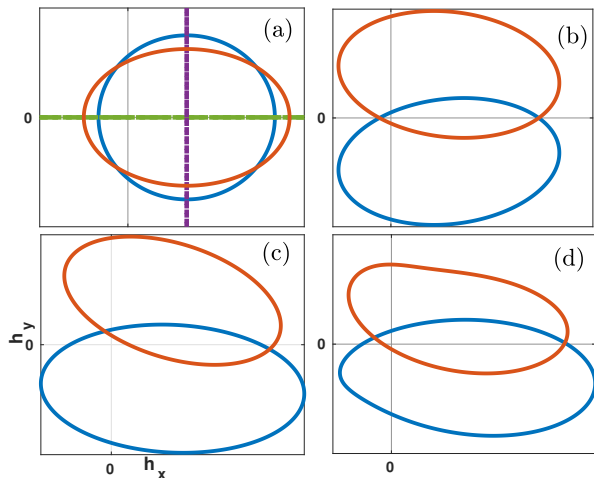


Figure 4. Here we show the generic shapes of the contour after eliminating ‘ $k$ ’ in  $h_x, h_y$  plane. Four distinct cases of interest are shown. In panel (a) shows circles (or ellipses) for up and down spin-sectors in brown and blue color respectively. Here all parameters are zero except  $v, w, \gamma$  i.e  $\eta = \eta_1 = \gamma_1 = \alpha_{R1} = \alpha_{R2} = 0, v = 2, w = 2.9, \gamma = 0.5$ . For  $w = \pm\gamma$ , the trajectory transforms into straight line along  $x$  and  $y$  axis as shown by magenta and green line respectively. In panel (b) we plot the contour for finite values of Rashba spin-orbit interaction(RSOI). The RSOI breaks the spin-degeneracies of the contours. However the winding number for each spin sector remains same. Values of  $\alpha_{R1}, \alpha_{R2}$  are 2 and 1.5 respectively. Panel (c) depicts effect of finite  $\eta$ . The contours for up and down spin sectors are now have different circumference length. In panel (d), we show effect of  $\gamma_1$  (a NNN hopping for  $v - w - v$  bonds as discussed). We note the changes in symmetry in the contour in comparison to the other cases discussed.

### B. General discussions on the parametric dependency of gapclosing point and other aspect

Now we proceed to discuss the parametric dependencies of gapclosing point and some other aspect in general which will help us to understand the role of each parameter in depth. We begin with the simple case of

$\gamma_1 = 0, \eta_1 = 0$  followed by other choices in turn.

**Case of  $\gamma_1 = 0, \eta_1 = 0$  :** In this case one can easily solve for  $\cos k$  and  $\sin k$  from Eqn 5 and 6. The condition  $\sin^2 k + \cos^2 k = 1$  yields the parametric equation in  $h_x - h_y$  plane. The solution for  $\cos k$  and  $\sin k$  for this choice are obtained as follows,

$$\sin k = \frac{-(w + \gamma)(h_y + \alpha_{R1}) + \alpha_{R2}(h_x - v)}{w^2 - \gamma^2 + \alpha_{R2}(\eta + \alpha_{R2})} \quad (7)$$

$$\cos k = \frac{(w - \gamma)(h_x - v) - \alpha_{R2}(h_y + \alpha_{R1}) - \eta(\alpha_{R1} + h_y)}{w^2 - \gamma^2 + \alpha_{R2}(\eta + \alpha_{R2})} \quad (8)$$

One can easily find the condition for the spectrum to be gapless by solving for ‘ $k$ ’ with  $h_x = h_y = 0$ . In general the parametric plot in  $h_x - h_y$  plane corresponds to ellipses of various shapes as shown in Fig. 4. For  $\alpha_{R1} = 0 = \alpha_{R2} = 0$ , we obtain the equation  $\frac{(h_x - v)^2}{(w + \gamma)^2} + \frac{h_y^2}{(w - \gamma)^2} = 1$  which is an ellipse. This particular scenario has been shown in panel (a) Fig. 4. We note that this choice of parameter makes both the spin sectors identical, Topological or non-topological. Similarly for  $\gamma = \eta = 0$ , one also finds that both the spin-sector obeys identical condition for the system to be topological or non-topological. This can be seen from the expression of  $\cos k$  at the gapless point (i.e  $h_x = h_y = 0$ ). We find  $\cos k = \frac{\alpha_{R1}\alpha_{R2} - vw}{w^2 + \alpha_{R2}^2}$  which remains identical as both  $\alpha_{R1}, \alpha_{R2}$  changes sign in going one spin-sector to other. However in the presence of both  $\gamma, \eta$  and  $\alpha_{R1}, \alpha_{R2}$ , the parametric plot of  $h(\vec{k})$  are different in  $h_x, h_y$  plane as before but now the two spin sectors obeys different conditions to be topological or not. Various cases corresponding to these are shown in panel (b), (c) and (d) in Fig. 4. This paves way to manipulate the topological character of each spin-sector individually. Now we explain the role played by  $\eta$ .

**Role of  $\eta$  :** It appears that  $\eta$  makes all the differences as it present itself in different combinations in spin-up and down sectors (See Eqn. 5, 6) To elucidate that we take the simple case of  $\gamma_1 = \eta_1 = 0$  which yield  $\cos k$  (with  $h_x = h_y = 0$ )  $\cos k = \frac{(\alpha_{R2} + \eta)\alpha_{R1} - v(w - \gamma)}{(w^2 - \gamma^2) + (\alpha_{R2} + \eta)\alpha_{R2}}$ . Here we note that a change of sign in  $\alpha_{R1}$  and  $\alpha_{R2}$  between the up-spin and down-spin sector makes the gapless condition to be different for up and down spin. As a result the topology of up-spin and down spin sectors are no longer tied with each other and may be different.

**Limit of  $\gamma = \pm w$  :** Another important limit is  $\gamma = \pm w$  where the gapless condition ( $h_x = h_y = 0$ ) turns out to be  $\cos k = -\frac{\alpha_{R1}}{\alpha_{R2}}$  which is independent of  $w, v$  and also remains same for both the spin sectors as  $\alpha_{R1}$  and  $\alpha_{R2}$  both changes sign from going one spin sector to other. This cases has been shown in panel (a) Fig. 4 by purple and green line.

**Role of  $\gamma_1$  and  $\eta_1$  :** From Eqn 5 and Eqn 6 we note that finite  $\gamma_1$  and  $\eta_1$  cause presence of  $\cos 2k$  and

$\sin 2k$  in the expressions of  $h_x$  and  $h_y$ . This does not allow easy solution for ‘ $k$ ’ for the gapclosing condition i.e  $h_x = h_y = 0$  at the topological transition point. However one can obtain a cubic equation for  $\cos k$  as explained in the Appendix and obtain the value for ‘ $k$ ’. Otherwise one may derive a transcendental equation by eliminating  $\sin 2k$  after multiplying Eqn. 5 (6) by  $\gamma_1(\eta_1/2)$  and then adding to obtain  $\mathcal{A}(k) = \mathcal{B}(k)$  with  $\mathcal{A}(k) = \gamma_1 h_x + \frac{\eta_1 h_y}{2} - \gamma_1^2 \cos 2k$  and  $\mathcal{B}(k) = \mathcal{B}_0 + \mathcal{B}_1 \cos k - \mathcal{B}_2 \sin k$  with  $\mathcal{B}_i$  being known function of the model parameter which are given by  $\mathcal{B}_0 = \gamma_1 v - \frac{\alpha_{R1}\eta_1}{2}$ ,  $\mathcal{B}_1 = \gamma_1(w + \gamma) + \frac{\alpha_{R2}\eta_1}{2}$  and  $\mathcal{B}_2 = \gamma_1(\eta + \alpha_2) + \frac{\eta_1}{2}(w - \gamma)$ . This is for up-spin only and analogous expressions for down spin can be easily obtained by changing the signs of  $\alpha_{Ri}$  and  $\gamma$ . One then can plot  $y_1(k) = \mathcal{A}(k)$  and  $y_2(k) = \mathcal{B}(k)$  to see whether there are any intersection for some ‘ $k$ ’. Interestingly if either  $\mathcal{B}_1$  or  $\mathcal{B}_2$  is zero for some choices of parameter, one obtains a quadratic equation for  $\cos k$  or  $\sin k$  which allows straight forward determination of gapless point and hence the transition point from topologically trivial to non-trivial region.

Having described the energy spectrum and the role of various parameters in detail and the criteria for the gap closing condition, we now proceed for topological characterizations of this hybrid SSH chain by investigating winding number for PBC and zero energy mid gap energy states for OBC.

### C. Topological characterization

We already mentioned that the system possesses a Chiral symmetry denoted by the operation  $S$ . This enables us to characterize the topology of the system by a winding number  $W$  which can take any integer value  $\mathbb{Z}$  [86–88]. The  $|\mathbb{Z}|$  yields the number of zero modes through bulk-boundary correspondence. For our purpose to calculate the winding number, it is useful to go in the Chiral basis through an unitary transformation such that the resulting Hamiltonian is block wise cross-diagonal as shown below.

$$\tilde{H}_{AB}(k) = U_S^\dagger \mathcal{H}(k) U_S = \begin{pmatrix} 0 & H_{AB}^+(k) \\ H_{AB}^-(k) & 0 \end{pmatrix}, \quad (9)$$

where, the unitary matrix  $U_S$  is such that  $U_{S_{ij}} = 1$  for  $i + j = 5$  only. Explicit expression of  $U_S$  and  $H_{AB}^+$  is given below

$$U_S = \begin{pmatrix} 0 & 0 & 0 & 1 \\ 0 & 0 & 1 & 0 \\ 0 & 1 & 0 & 0 \\ 1 & 0 & 0 & 0 \end{pmatrix}, \quad H_{AB}^+ = \begin{pmatrix} \lambda_+(k) & 0 \\ 0 & \lambda_-(k) \end{pmatrix} \quad (10)$$

with  $\lambda_{\pm}(k) = v \pm i\alpha_{R1} + e^{ik} \left( w - i\left(\frac{\xi}{2} - \pm\alpha_{R2}\right) \right) + e^{-ik}(\gamma + i\frac{\eta}{2}) + e^{i2k}(\gamma_1 + i\frac{\eta_1}{2})$ . Using  $H_{AB}^{\pm}(k)$ , one can

define the winding number  $W (\in \mathbb{Z})$  as [86, 87]

$$W = \left\lfloor \pm \frac{i}{2\pi} \int_{-\pi}^{\pi} dk \text{Tr} \left[ \{H_{AB}^{\pm}(k)\}^{-1} \partial_k H_{AB}^{\pm}(k) \right] \right\rfloor. \quad (11)$$

Having defined the winding number we now proceed to discuss various topological phases that we obtain by evaluating Eqn. 11 numerically. We first begin with the simple case where  $\tilde{\gamma}$  is zero followed by the finite  $\tilde{\gamma}$ . Before delving into details we note that the salient characteristic of the system is that depending on the parameters, the winding number of each spin sector can be anything making the possible winding number for the whole system to be 0, 1, 2 as shown in Fig. 5. Here a density plot of winding number has been presented in ‘ $w - v$ ’ plane. In panel (b) and (d), the parameters are chosen such that we obtain winding number 0 or 2 implying both the spin-sector has identical winding number. In panel (a) and (c), the winding number could be 0, 1, 2. Remarkably in both of these panel we find a re-entrant topological region with winding number one and interestingly panel (c) present a multi-critical point where all the possible topological phases. Now we proceed to explain in detail how such different topological phases arises for this hybrid SSH chain.

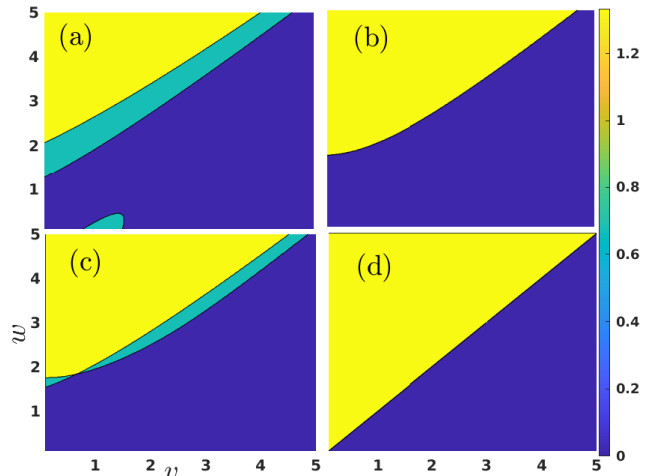


Figure 5. Density plot of winding number are presented in  $w-v$  plane. The blue, cyan and yellow region correspond  $W = 0, 1, 2$  respectively. In the upper left corner we have shown how winding number changes as ‘ $w$ ’ varies depending on various set of parameters. In panel (a), (b), (c), (d) the set of parameters correspond to  $(\eta, \alpha_{R1}, \alpha_{R2}, \gamma) = (0.0, 0.0, 0.0, 0.05)$ ,  $(0.0, 2.0, 1.0, 0.0)$ ,  $1, 2.0, 1.0, 0.0$  and  $1, 2.0, 1.0, 1.5$  respectively. We note the re-entrant topological phase transition in panel (a) and (c).

For that we note that the tight binding model as given in Eq. 2 can also be written for each spin channel as  $\mathbf{h}_\sigma = \sum_k h_{\sigma,x}(k)\sigma_x + h_{\sigma,y}(k)\sigma_y$  with  $h_{\sigma,\alpha}(k)$  given in Eqn. 5 and 6 with  $\sigma = \uparrow, \downarrow$ . For proceeding further, we

rewrite Eqn. 5 and 6 explicitly for up and down spin sector with  $\xi = -\eta$  substitution.

$$h_{x,\uparrow} = v + (\eta - \alpha_{R2}) \sin k + (w + \gamma) \cos k + \gamma_1 \cos 2k - \frac{\eta_1}{2} \sin 2k \quad (12)$$

$$h_{y,\uparrow} = \alpha_{R1} + (w - \gamma) \sin k + \alpha_{R2} \cos k + \gamma_1 \sin 2k + \frac{\eta_1}{2} \cos 2k \quad (13)$$

$$h_{x,\downarrow} = v + (\eta + \alpha_{R2}) \sin k + (w + \gamma) \cos k + \gamma_1 \cos 2k - \frac{\eta_1}{2} \sin 2k \quad (14)$$

$$h_{y,\downarrow} = -\alpha_{R1} + (w - \gamma) \sin k - \alpha_{R2} \cos k + \gamma_1 \sin 2k + \frac{\eta_1}{2} \cos 2k \quad (15)$$

Though the above expressions are written for general cases in below we only discuss special cases which restore enhanced algebraic simplification of the resulting equations without loss of generality and hence helps us to explain symmetry protected topological phases.

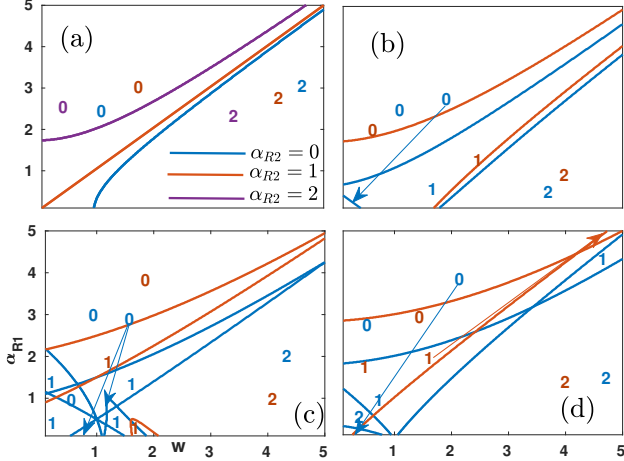


Figure 6. Phase diagram in  $\alpha_{R1} - w$  plane. Different colored lines separate two different topological phases (which are represented by winding numbers of same color) for a given set of parameters. Values of  $\alpha_{R2}$  are taken as 0, 1, 2 as denoted in panel (a) and color code is same for other panels. For different panel the set of parameters  $\eta, \eta_1, \gamma, \gamma_1$  are taken as (0.0, 0.0, 0.0, 0.0), (2.0, 0.0, 0.5, 0.0), (1.0, 1.0, 1.5, 1.5) and (2.0, 2.0, 0.5, 0.5) for panel (a), (b), (c) and (d) respectively. In panel (b), (c) and (d) we notice re-entrant topological phases which are shown by arrows.

### 1. Role of finite $\alpha_{R1}$ and $\alpha_{R2}$ but $\gamma = \eta = 0$

We first discuss the role of finite Rashba interaction in the absence of  $\gamma_i, \eta_i$ . We note that this parameter choice is characterized by the following symmetry (See Eqn. 12 to Eqn. 13), under  $k \rightarrow -k$ ,

$$\{h_{x\uparrow}(k) \rightarrow h_{x\downarrow}(k), \quad h_{y\uparrow}(k) \rightarrow -h_{y\downarrow}(k)\} \quad (16)$$

The original (spinless) SSH model is known to possess topologically non-trivial phase with winding number  $W = 1$  for  $w > v$  and one topologically trivial phase with winding number  $W = 0$  for  $w < v$ . For  $\tilde{\gamma}_i = 0$  and finite Rashba interaction effective  $w$  and  $v$  become complex and acquire different functional form for each spin sectors with  $w_\uparrow = w + i\alpha_{R1}$ ,  $w_\downarrow = w + i\alpha_{R2}$  and  $v_\uparrow = v - i\alpha_{R1}$ ,  $v_\downarrow = v - i\alpha_{R2}$ . One may rewrite this as  $w_\uparrow = |w|_\uparrow e^{i\theta}$ ,  $w_\downarrow = |w|_\downarrow e^{-i\theta}$  and  $v_\uparrow = |v|_\uparrow e^{i\zeta}$ ,  $v_\downarrow = |v|_\downarrow e^{-i\zeta}$ . We notice that the magnitude of effective intercell and intracell hopping change equally for both the spin sectors. The modified dispersion yields  $\epsilon_\sigma = ||v|_\sigma + |w|_\sigma e^{i(k+\zeta-\theta)}|$ . The above relation shows that the location of zeros at the topological phase transition point changes for two spin sectors simultaneously for a given  $\alpha_{R1}, \alpha_{R2}, v, w$  and importantly if it happens for some values of  $\alpha_{R1}$  and  $\alpha_{R2}$ , we have  $|v_\sigma| > |w_\sigma|$ , the topological nature can be changed from non-trivial to trivial phases. However we note that this happens simultaneously for both the spin sectors. As a result we only obtain winding number either zero(0) or two(2) as shown in Fig. 5, panel (b,d) and in Fig. 6, panel (a) and in Fig.7 panel (b).

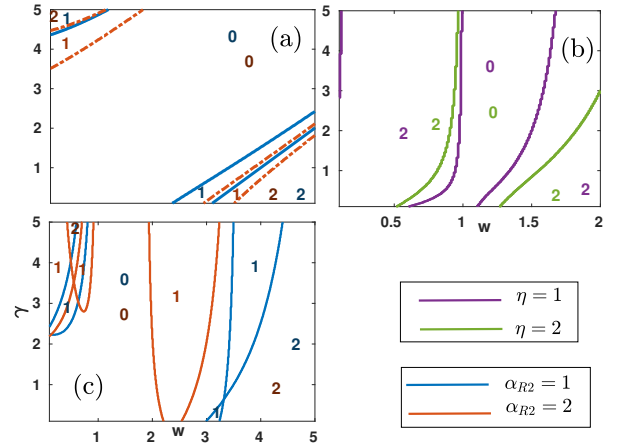


Figure 7. Phase diagrams are plotted in  $\gamma - w$  plane for different set of parameters. In panel (a), we have taken  $\eta = 1, \alpha_{R1} = 3, \eta = 0, \gamma_1 = 0$ . For panel (b) and (c) we have taken  $\gamma_1 = \gamma$ . For panel (b),  $\alpha_{R1}$  and  $\alpha_{R2} = 0$  and blue and brown color represents  $\eta = 1$  and 2 respectively. In panel (c) we used  $\eta = 1, \alpha_{R1} = 3$  and brown and blue curves represent  $\alpha_{R2} = 1$  and 2 respectively.

### 2. Role of finite $\alpha_{R1}, \alpha_{R2}$ and $\eta = 0$ but finite $\gamma$

Now we examine the role of finite but real  $\gamma, \gamma_1$ . From Eqn. 12 to Eqn. 15, we find that, for this choice of parameters we also have the following mapping between the up and down spin sectors under  $k \rightarrow -k$ ,

$$\{h_{x\uparrow}(k) \rightarrow h_{x\downarrow}(k), \quad h_{y\uparrow}(k) \rightarrow -h_{y\downarrow}(k)\} \quad (17)$$

The above mapping suggests that the topological phases of both the spin sector are tied to be identical to each other i.e the topological phase we obtain are with  $W = 0$  or  $2$ . This has been shown in Fig. 5, panel (b). However though the winding number of each spin sector are identical to each other, the contour they make in  $h_x - h_y$  plane are not identical which can be understood as follows. Presence of  $\gamma$  yields the modified expressions for  $\vec{h}_\sigma$  as explained. For the up spin sector,  $\vec{h}_{x\uparrow} = v + w \cos(k + \theta_\uparrow) + (\gamma_1 \cos k + \gamma_2 \cos 2k)$ ,  $\vec{h}_{y\uparrow} = w \sin(k + \theta_\uparrow) + (\gamma_1 \sin k + \gamma_2 \sin 2k)$ . For the down spin sector we have,  $\vec{h}_{x\downarrow} = v + w \cos(k + \theta_\downarrow) + (\gamma_1 \cos k + \gamma_2 \cos 2k)$ ,  $\vec{h}_{y\downarrow} = w \sin(k + \theta_\downarrow) + (\gamma_1 \sin k + \gamma_2 \sin 2k)$ . This suggests that the presence of different  $\theta_\sigma$  for each spin sectors may give rise to different closed contour due to the presence of  $\gamma_1$  and  $\gamma_2$ . Unlike the previous case, the tip of the vector  $\vec{h}_\sigma$  does not lie on the same circle but give rise to two different closed contour as shown in Fig. 4, panel(b).

### 3. Role of finite $\alpha_{R1}$ , $\alpha_{R2}$ and finite $\eta$ i.e finite $\tilde{\gamma}$

For this parameter choices, one finds that, under  $k \rightarrow -k$

$$\{h_{\uparrow,x}(k) \neq h_{\downarrow,x}(k), \quad h_{\uparrow,y}(k) \neq h_{\downarrow,y}(k)\} \quad (18)$$

To elucidate the parametric interplay of  $v, w, \gamma_1, \gamma_2$  in a simpler way, we substitute  $\tilde{w} = w + i\eta/2$ ,  $\tilde{\gamma}_1 = \gamma - i\eta/2$ . Specifically, when both intercell hopping and next-to-next-nearest-neighbor hopping contribute real values along with RSO interactions, the winding number is 0 or 2 depending on some critical value of  $w_c$  which is determined by given  $v, \alpha_{R1}, \alpha_{R2}$ , as shown in Fig. 5, panel(b). However, if the imaginary part of intercell hopping and next-to-next-nearest-neighbor hopping also contribute in the presence of RSO interaction, the winding number changes from  $0 \rightarrow 1 \rightarrow 2$  due to the in-equivalence of two spin-sectors as given in Eq. 18. Thus the presence of the multiple-phase transition (where  $W$  takes  $1 \rightarrow 0 \rightarrow 1 \rightarrow 2$ ) becomes evident when both imaginary hopping and Rashba spin-orbit interaction (RSOI) are simultaneously present. In Fig. 5 panel (c), in Fig. 6 panel (b), (c), (d) and in Fig. 7 panel (a), (c) we have shown such scenario. We have checked that for the choice  $\tilde{w} = w - i\eta/2$ ,  $\tilde{\gamma}_1 = \gamma + i\eta/2$ , the above description of topological phase remains same. It is also valid for  $\tilde{w} = w - i\eta/2$ ,  $\tilde{\gamma}_1 = \gamma + i\eta'/2$  with  $\eta \neq \eta'$  but for simplicity we have considered  $\eta = \eta'$ . Thus the condition  $h_{\uparrow,x}(k) \neq h_{\downarrow,x}(k')$ ,  $h_{\uparrow,y}(k) \neq h_{\downarrow,y}(k')$  for any  $k$  and  $k'$  is the sufficient condition to have different winding number for each spin sector and it is one of our main result. The physical reason is that simultaneous presence of Rashba and imaginary  $w$  and  $\gamma$  does not allow the up-spin Hamiltonian to be mapped to down-spin Hamiltonian for any

' $k$ '.

### 4. Role of vanishing $\alpha_{R1}$ and $\alpha_{R2}$ but finite $\eta$ i.e finite $\tilde{\gamma}$

For this choice of parameter we also have the following mapping between the up and down spin sector under  $k \rightarrow -k$ ,

$$\{h_{\uparrow,x} = h_{\downarrow,x}, \quad h_{\uparrow,y} = h_{\downarrow,y}\} \quad (19)$$

From the conclusion of previous discussion, it is obvious that for this case the topological phases of both the spin sector is identical i.e winding number is either 0 or 1. This case has been plotted in Fig. 7 panel (b).

### D. Bulk boundary correspondence

It is well known that the non-trivial topology of a system is guaranteed by a bulk invariant for periodic boundary condition and associated edge mode for open boundary system. For one dimensional system the edge modes are localized at the two open edges with decaying amplitude as we go inside the bulk from edges. For all the finite winding number we find appropriate edge modes as expected. For completeness in Fig. 8 we show appearances of mid gap zero energy modes for representative parameters. In Fig. 8 we show mid gap zero energy modes for winding number 1 (in panel (a)) and 2 (in panel (b)). These corresponds to the topological phases with finite winding number  $W=1$  and 2 as shown in panel (c). The relevant parameters are displayed at lower right inset.

As we are dealing with many parameters it is pertinent to ask how the profile of each edge modes corresponding to each finite value of winding number does depend on parameters. While it is known that for each cases the probability amplitude at the extreme edge which we number as  $N = 0$  site, (i.e  $|\Psi_0|^2$ ) is maximum and it decays inside. Thus it may be of interest to investigate how the profile of the probability amplitude  $|\Psi_N|^2$  depends on parameter. This may be of practical importance to look for stability of edge-modes against interactions or coupled chains when inter-chain coupling could have spatial dependence. To this end in Fig. 9 we have plotted  $|\Psi_N|^2$  or  $N = 12$  (counted from the edge toward the bulk). In panel (a), we have shown how it depends on  $\gamma$  for  $\eta = 1, 2, 3$  and other parameters (see caption in Fig. 9). We notice a non-monotonous dependence with a critical value of  $\gamma_c$  at which the amplitude  $|\Psi_{12}|^2$  is locally maximum, it then decreases with  $\gamma$  and then finally increases again.  $\gamma_c$  decreases with increase in  $\eta$ . From the panel (b), we notice that  $|\Psi_{12}|^2$  decreases almost monotonously as we increase  $\alpha_{R2}$  for a given  $\gamma$  and saturates for large  $\alpha_{R2}$ . However for low values of  $\alpha_{R2}$ ,  $|\Psi_{12}|^2$  increases

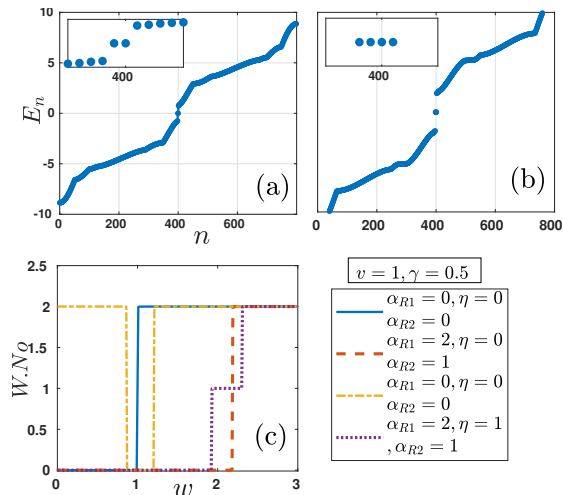


Figure 8. Eigenvalues are plotted for open chain of 800 sites for representative parameters. For panel (a) and panel (b) we considered  $w = 2$  and  $4$  respectively. For other parameters we have taken  $\alpha_{R1} = 3, \alpha_{R2} = 2, \gamma = \gamma_1 = 0.5, \eta = \eta_1 = 3, v = 1$ . Panel (a) and (b) correspond  $W = 1$  and  $2$  respectively as evident from the single and double pair pair of mid gap zero energy mid gap states shown in the inset. In panel (c), we have shown winding number vs  $w$  for different representative set of parameters denoted in the right lower panel.

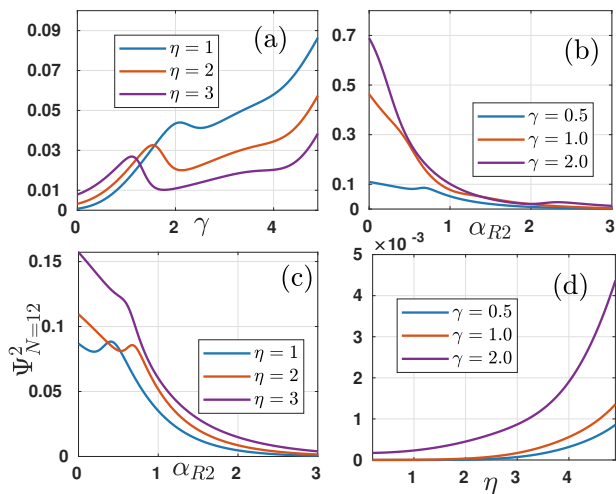


Figure 9. Probability amplitude of zero energy edge modes at site  $N = 12$  counted from the edge toward bulk are plotted for various parameters. For each plot we have used  $v = 1, w = 4, \alpha_{R1} = 3$ . Panel (a) shows variance with  $\gamma$  for  $\eta = 1, 2, 3$  with  $\eta = \eta_1, w = \gamma = \gamma_1, \alpha_{R2} = 2$ . Panel (b) shows variance with  $\alpha_{R2}$  for  $\gamma = 0.5, 1.0, 2.0$  with  $\eta = \eta_1 = 2, \gamma = \gamma_1$ . Panel (c) shows variance with  $\alpha_{R2}$  for  $\eta = 1, 2, 3$  while  $\eta = \eta_1, \gamma = \gamma_1 = 0.5$ . Panel (d) shows variance with  $\eta$  for  $\gamma = 0.5, 1.0, 2.0$  while  $\eta = \eta_1, \gamma = \gamma_1, \alpha_{R2} = 2$ . Here we have taken an open chain with  $N = 100$  sites.

with increase in  $\gamma$  which shows the NNNN hopping favors the localization of wave function more towards the bulk as expected. In panel (c) we see similar behavior as in panel (b) which is expected as effect of  $\eta$  is similar to

$\gamma$ , both being responsible for NNNN hopping. In panel (d) we plot how the amplitude depends on  $\eta$  for various  $\gamma$  (both being responsible for NNNN hopping) for a given set of other parameters. It appears that as we increase  $\eta$  for a given  $\gamma$ ,  $|\Psi_{12}|^2$  monotonously increases (which is opposite to the case in panel (a)). Again, for a given  $\eta$ ,  $|\Psi_{12}|^2$  increases for increase in  $\gamma$ . This shows a contrasting behavior and different dependency of  $|\Psi_{12}|^2$  on  $\eta$  ( $\gamma$ ) for a fixed  $\gamma$  ( $\eta$ ).

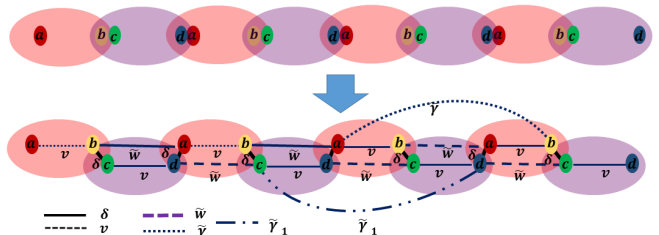


Figure 10. A cartoon picture of two coupled SSH chains are shown in two different way. The upper panel pink and magenta denote the unit cell of each SSH chain where (a,b) sites belong to first chain and (c,d) sites belong to second chain. the coupling between two chains are denoted by a hopping  $\delta$  between the ‘b’-sublattice of first chain to ‘c’ sublattice of second chain. All other intrachain hopping for single SSH chain considered previously remains same for both the chains. We note that sites ‘c’ and ‘d’ of the second chain are equivalent sub-lattices of ‘a’ and ‘b’ in the first chain.

### III. TWO AND FOUR SSH CHAIN WITH RSOI AND INTER CELL HOPPING

Having described the various topological properties of single chain extended SSH Hamiltonian elucidating the role of different parameters on how they modify the topology, we now move on to investigate few such coupled chains and its consequences. In our scheme, chains are connected by a real coupling  $\delta$  which allows only inter sub-lattice hopping between the chains such as to preserve the Chiral symmetry as shown in Fig. 10 and Fig. 14. We have only considered two and four coupled SSH chain. We begin our discussion with two coupled SSH chain..

#### A. Detailed analysis of two coupled SSH chains

The coupling between two SSH chain can be represented by the inter-chain Hamiltonian as given below,

$$H_c = \delta \sum_{n=i}^N \left( \psi_{1,n,d}^\dagger \psi_{2,n,\bar{d}} + \text{h.c.} \right) \quad (20)$$

In the above ‘1’ and ‘2’ denotes the first and second chains respectively.  $d$  and  $\bar{d}$  denote the sublattice indices  $a$  and  $b$  such that  $d \neq \bar{d}$  as shown in Fig. 10. After



a straightforward Fourier transform and taking into account the intra-chain Hamiltonian  $H_1$  and  $H_2$  for isolated SSH chain where indices ‘1’ and ‘2’ refer the upper and lower chain respectively, we can re-write the complete Hamiltonian for two coupled SSH chains as given below,

$$H_{2c} = \sum_k \left( h_{1,k} \xi_{1,a,k}^\dagger \xi_{1,b,k} + \text{h.c.} \right) + \left( h_{2,k} \xi_{2,a,k}^\dagger \xi_{2,b,k} + \text{h.c.} \right) \\ + \sum_k \left( h_{3,k} \xi_{3,a,k}^\dagger \xi_{3,b,k} + \text{h.c.} \right) + \left( h_{4,k} \xi_{4,a,k}^\dagger \xi_{4,b,k} + \text{h.c.} \right) \quad (21)$$

Where  $h_{1,k} = J_1(k) + \delta$ ,  $h_{2,k} = J_2(k) - \delta$ ,  $h_{3,k} = J_1(k) - \delta$ ,  $h_{4,k} = J_2(k) + \delta$ . Various  $\xi$ 's are defined as  $\xi_{1,a} = (-\psi_{1,b,\downarrow} + \psi_{2b\downarrow})$ ,  $\xi_{1,b} = (-\psi_{1,a,\downarrow} + \psi_{2a\downarrow})$ ,  $\xi_{2,a} = (\psi_{1,b,\uparrow} - \psi_{2b\uparrow})$ ,  $\xi_{2,b} = (\psi_{1,a,\uparrow} - \psi_{2a\uparrow})$ ,  $\xi_{3,a} = (\psi_{1,b,\downarrow} + \psi_{2b\downarrow})$ ,  $\xi_{3,b} = (\psi_{1,a,\downarrow} + \psi_{2a\downarrow})$ ,  $\xi_{4,a} = (\psi_{1,b,\uparrow} + \psi_{2b\uparrow})$ ,  $\xi_{4,b} = (\psi_{1,a,\uparrow} + \psi_{2a\uparrow})$ . In Eq. 21  $\xi_{i,\alpha,k}$ 's are redefined fermionic operators in terms of the original fermions  $\psi_{1,a,\sigma}$ ,  $\psi_{1,b,\sigma}$ ,  $\psi_{2,a,\sigma}$ ,  $\psi_{2,b,\sigma}$  where 1 and 2 indicate the chain indices,  $a$  and  $b$  sub-lattice indices and  $\sigma$  spin indices. Thus it is clear that  $\xi_{i,\alpha,k}$ 's are various symmetric and anti-symmetric combinations of the original fermions  $\psi_{i,\alpha,\sigma}$ . This will help us to understand the effect of coupling and explain the consequences.  $J_1(k)$  and  $J_2(k)$  are the spectral function for the single-chain extended SSH Hamiltonian as given in Eq. 5 and Eq. 6. Here ‘1’ and ‘2’ refer up and down spin respectively. A comparison of  $h_1$  and  $h_2$  in Eq. 21 with the expression of  $h_\uparrow$  and  $h_\downarrow$  in Eq. 5 and Eq. 6 We note that the effect of  $\delta$  is manifested in re-normalizing the intra-sublattice hopping with values  $v \pm \delta$ . Thus we expect criteria for non-trivial topology to have different dependencies on parameters than the single chain. Depending on the sign and magnitude of  $\eta$ ,  $\delta$  and  $w$ , the various  $\xi$  sectors can be made topological or non-topological. In the table I we enumerates in details the relative signs of  $\eta$ ,  $\delta$  and value of  $w$  for which various fermionic sectors can be made topological. From the table we note that as we increase the value of inter-cell hopping, multiple  $\xi$ -sectors could be made topological. In order to minimize the dependencies on multiple parameters, we have maintained the constancy of all parameters except for the intercell hopping parameter  $w$ . However for a given value of ‘ $w$ ’ the sign of  $\eta$  and  $\delta$  is important for a given sectors to be topological. This understanding allows us to manipulate the topology of a given sector by controlling the sign of  $\delta$ ,  $\eta$  and magnitude of  $w$  and could pave way of realizing quantum gates.

The Hamiltonian as expressed in Eq. 21 is not manifestly Chiral invariant. The Chiral basis can be obtained in the original  $\psi$  basis be defining  $(\Psi_{12}^\dagger = (\Psi_1^\dagger \Psi_2^\dagger))$  with  $\Psi^\dagger$  defined after Eq. 1 ) and rewriting the Hamiltonian

W=1	$\eta$	$\delta$	$w$
$\xi_3$	+	+	$w_1$
$\xi_2$	+	-	$w_1$
$\xi_1$	-	+	$w_1$
$\xi_4$	-	-	$w_1$
W=2			
$\xi_2, \xi_3$	+	$\pm$	$w_2 > w_1$
$\xi_1, \xi_4$	-	$\pm$	$w_2 > w_1$
W=3			
$\xi_2, \xi_3, \xi_4$	+	+	$w_3 > w_2 > w_1$
$\xi_1, \xi_2, \xi_3$	+	-	$w_3 > w_2 > w_1$
$\xi_1, \xi_2, \xi_4$	+	+	$w_3 > w_2 > w_1$
$\xi_1, \xi_3, \xi_4$	+	-	$w_3 > w_2 > w_1$
W=4			
$\xi_1, \xi_2, \xi_3, \xi_4$	$\pm$	$\pm$	$w_4 > w_3 > w_2 > w_1$

Table I. The table depicts how the winding number depends on the signs of  $\eta$ ,  $\delta$  and magnitude of  $w$ . Also the first column depicts the normalized fermionic sectors which has finite winding number.

as,

$$\mathcal{H}_{12}(k) = [v + (w + \gamma) \cos k - \eta \sin k] \Gamma_5 - (w - \gamma) \sin k \Gamma_6 \\ + [\alpha_{R1} - \alpha_{R2} \cos k] \Gamma_7 - \alpha_{R2} \sin k \Gamma_8 + \delta \Gamma_9 \quad (22)$$

where  $\Gamma$  is a  $8 \times 8$  matrix given as  $\Gamma_5 = \sigma_0 \otimes \sigma_x \otimes \sigma_0$ ,  $\Gamma_6 = \sigma_0 \otimes \sigma_y \otimes \sigma_0$ ,  $\Gamma_7 = \sigma_0 \otimes \sigma_y \otimes \sigma_x$ ,  $\Gamma_8 = \sigma_0 \otimes \sigma_x \otimes \sigma_z$  and  $\Gamma_9 = \sigma_x \otimes \sigma_x \otimes \sigma_0$ . One can now easily check that the Hamiltonian Eq.(22) preserves the chiral symmetry and the corresponding operator has the form  $S = \sigma_0 \otimes \sigma_z \otimes \sigma_0$  yielding  $S^{-1} \mathcal{H}_{12}(k) S = \mathcal{H}_{12}(-k)$ .

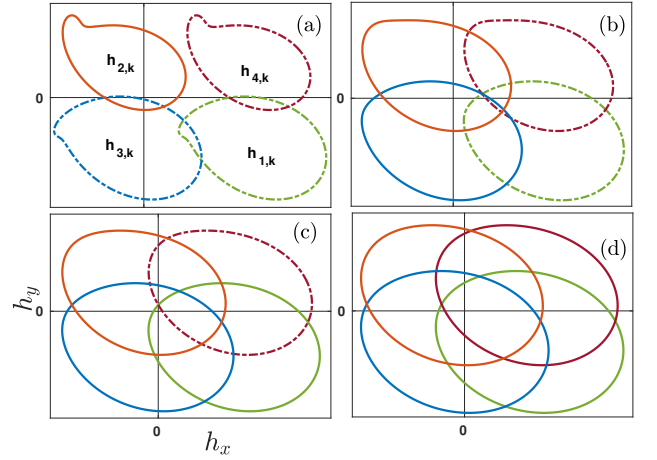


Figure 11. The tip of the vector  $(\vec{h}(k)_x, \vec{h}(k)_y)$  are plotted to show the topological origin of zero energy mid gap states. The four different contours correspond different  $\xi_i$  sectors as represented by  $h_{i,k}$  in panel (a). The four panel (a), (b), (c) and (d) correspond two, four, six and eight mid gap states respectively. Here for all panels  $v = 0.2$ ,  $\alpha_{R1} = 0.3$ ,  $\alpha_{R2} = 0.1$ ,  $\gamma = \gamma_1 = 0.05$ ,  $\eta = 0.2$ ,  $\delta = 0.4$ . For panel (a), (b), (c) and (d) value of  $w$  is 0.3, 0.5, 0.7, 0.9 respectively.

To determine the topological invariant of two-coupled SSH chain, we convert the Hamiltonian given in Eq. 22 in off-diagonal block form with the following operation given below.

$$\begin{aligned}\tilde{H}_{A-D}(k) &= U^\dagger_S \mathcal{H}_{12}(k) U_S \\ &= \begin{pmatrix} 0 & H_{A-D}^+(k) \\ H_{A-D}^-(k) & 0 \end{pmatrix},\end{aligned}\quad (23)$$

where, the Chiral-basis are used to construct the unitary matrix  $U_S$  which is given in the Appendix.  $H_{A-D}^\pm(k)$  are  $4 \times 4$  square matrices, defined on the  $\pm$  chiral block, respectively. Using  $\mathcal{H}_{A-D}^\pm(k)$ , afterward, Winding number is calculated using Eq.11. Explicit expressions of  $U_S$  and  $\mathcal{H}_{A-D}^\pm(k)$  are given in Appendix.

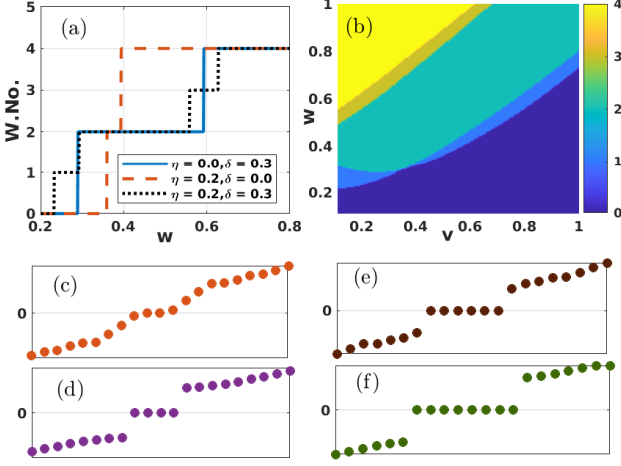


Figure 12. In panel (a) we plot winding number vs  $w$  for different values of other parameters as given in the inset. One note that all possible winding numbers are obtained depending on the parameters. In panel (b) a density plot of winding number is presented in  $w-v$  plane for  $\eta = 0.2, \delta = 0.3, \gamma = \gamma_1 = 0.05, \alpha_{R1} = 0.3, \alpha_{R2} = 0.1$ . We observe that all possible winding number i.e 0,1,2,3,4 are obtained. In panel (c,d,e,f) we plot the LDOS corresponding to winding number 1,2,3,4 respectively corresponding to different regions of finite winding number in panel (b).

Fig. 12 illustrates the plot for the winding number. In Fig. 12, the plot depicts the winding number as a function of intercell hopping  $w$ . We observe that the winding number can take on values of 4,3, 2, 1, or 0, depending on the strengths of the Rashba spin-orbit interaction (RSOI), intercell hopping, intracell hopping, and next-to-next-nearest-neighbor hopping and interchain hopping. Moreover as ' $w$ ' is increased, winding number takes higher integer values gradually. In Fig. 12 panel (b) we show density plot for winding number in  $w-v$  plane for certain set of parameters ( $\eta = 0.2, \delta = 0.3, \gamma = \gamma_1 = 0.05, \alpha_{R1} = 0.3, \alpha_{R2} = 0.1$ ) such that all possible winding numbers are obtained in  $w-v$  plane. In panel (c), (d), (e) and (f), we plot the appearances of mid-gap zero energy states for an open coupled-chain of 800 sites. We conclude the study of

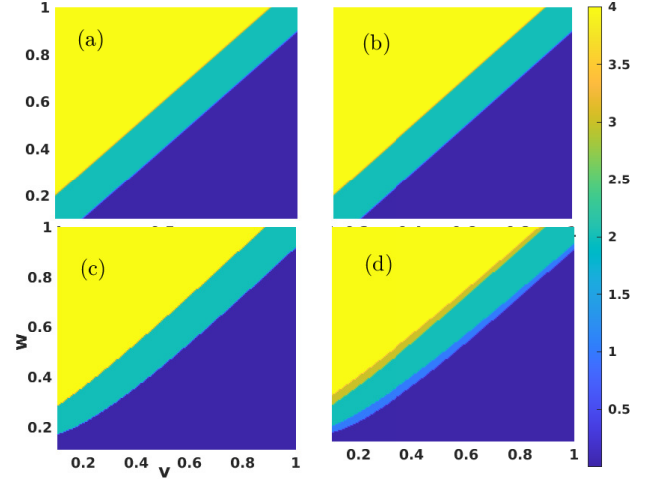


Figure 13. Additional density plot of winding number for two coupled SSH chain in  $w-v$  plane are shown. The parameters set taken in different panel are as follows. Panel (a) corresponds  $\eta = \eta_1 = \gamma = \gamma_1 = \alpha_{R1} = \alpha_{R2} = 0, \delta = 0.1$ . Panel (b) corresponds to  $\eta = \eta_1 = \alpha_{R1} = \alpha_{R2} = 0, \delta = 0.1, \gamma = \gamma_1 = 0.05$ . For panel (c), we take  $\alpha_{R1} = 0.2, \alpha_{R2} = 0.1, \gamma = 0.05, \delta = 0.1$ . Finally panel (d) refers  $\alpha_{R1} = 0.2, \alpha_{R2} = 0.1, \gamma = 0.005, \delta = 0.1, \eta = 0.1$ .

two-coupled chain study by presenting an additional set of contour plot of winding number in  $w-v$  plane for various set of parameters as shown in Fig. 13. Panel (a) shows the effect of  $\delta$  when all other parameters are zero. We find that the region  $w - \delta < v < w + \delta$  is non topological. The region with  $w + \delta > v > w - \delta$  contains topological phase with winding number one and the region  $w + \delta$  corresponds winding number 2. This explains the role played by  $\delta$ . For  $\delta = 0$ , we recover the SSH chain phase boundary for  $w = v$  straight line. Fig. 13 panel (b), (c) and (d) show the effect of other parameters being finite. Notably as seen from panel (b), a finite small  $\gamma = \gamma_1 = 0.05$  does not change the phase boundary qualitatively and it remains linear. However as one turns on finite  $\alpha_{Ri}$ , the phase boundary becomes non-linear for small  $v$  and  $w$  as seen in panel (c). However the panel (a), (b) and (c) has only topological phases with even winding number. In Fig. 13 panel (d) we show phase diagram with finite  $\eta$  yielding all possible winding numbers.

## B. Detailed analysis of four coupled SSH chains

As seen from the above work that two interconnected SSH chains gives a wide range of topological phases. Thus the natural questions arises what if we increases the number of chains and whether the above realization of arbitrary winding number holds. Motivated by this we increases the number of chains to four. The connection between the neighboring chains follows the same scheme i.e it always connect different in equivalent sublattices to preserve the chiral symmetry. This has been elucidated

in Fig.14. The Hamiltonian  $H_{4c}$  for the four chain model

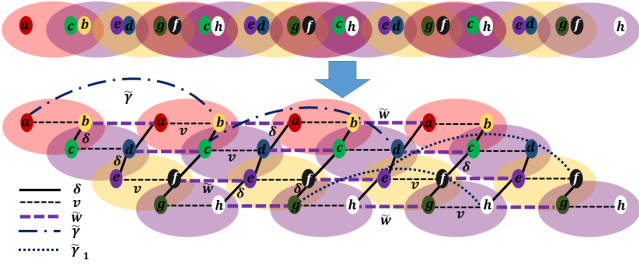


Figure 14. A cartoon picture of four coupled SSH chains is shown in two different equivalent representation. In the upper panel, the pink, light magenta, yellow, and deep magenta denotes the unit cells of each individual SSH chain with sublattices  $(a, b)$ ,  $(c, d)$ ,  $(e, f)$  and  $(g, h)$  respectively. For each chain the first and second alphabets denotes the equivalent sub-lattices for each chain. The interchain coupling are always between two in-equivalent sub-lattices between neighboring chain.

is given in Eq.24. Here  $H_{ab}$ ,  $H_{cd}$ ,  $H_{ef}$  and  $H_{gh}$  are the Hamiltonian for each single chain given in Eq. 1 and  $(\mu\nu)$  in  $H_{\mu\nu}$  denotes the equivalent sub-lattices in each chain.

$$H_{4c} = H_{ab} + H_{cd} + H_{ef} + H_{gh} + H_{a \rightarrow h} \quad (24)$$

In the above  $H_{a \rightarrow h}$  denotes the coupling terms between two neighboring chain and we are considering periodic boundary condition. Explicitly, we have

$$H_{a \rightarrow h} = \delta \sum_{n=i}^N [\psi_{n,\mu}^\dagger \psi_{n+1,\nu'} + \psi_{n,\nu}^\dagger \psi_{n+1,\mu'} + h.c], \quad (25)$$

where ‘ $n$ ’ denotes the  $n$ -th chain and  $(\mu, \nu)$  and  $\mu', \nu'$  denote the pair of equivalent sublattices of neighbouring chains. We perform Fourier transform to obtain for  $H_{4c}$ ,

$$H_{4c} = [v + (w + \gamma) \cos k - \eta \sin k] \Gamma_{10} - (w - \gamma) \sin k \Gamma_{11} + [\alpha_{R1} - \alpha_{R2} \cos k] \Gamma_{12} - \alpha_{R2} \sin k \Gamma_{13} + \delta \Gamma_{14} \quad (26)$$

where  $\Gamma$  is a  $16 \times 16$  matrix given as  $\Gamma_{10} = \sigma_0 \otimes \sigma_0 \otimes \sigma_x \otimes \sigma_0$ ,  $\Gamma_{11} = \sigma_0 \otimes \sigma_0 \otimes \sigma_y \otimes \sigma_0$ ,  $\Gamma_{12} = \sigma_0 \otimes \sigma_0 \otimes \sigma_y \otimes \sigma_x$ ,  $\Gamma_{13} = \sigma_0 \otimes \sigma_0 \otimes \sigma_x \otimes \sigma_z$ ,  $\Gamma_{14} = \sigma_0 \otimes \sigma_x \otimes \sigma_x \otimes \sigma_0 + (\sigma_x \otimes \sigma_x \otimes \sigma_0 + \sigma_y \otimes \sigma_y \otimes \sigma_x \otimes \sigma_0)/2$ . The Hamiltonian Eq.(26) preserves the chiral symmetry with the following symmetry operator  $S'' = \sigma_0 \otimes \sigma_z \otimes \sigma_0 \otimes \sigma_0$ :  $S''^{-1} H(k)_{4c} S'' = -H_{4c}(k)$ .

To study the topological properties of four coupled chain system, we first re-cast our Hamiltonian  $H_{4c}$  in a manifestly off-diagonal block form with the help of operator  $U_{S''}$  as follows.

$$\begin{aligned} \tilde{H}_{A-H}(k) &= U_{S''}^\dagger H_{4c}(k) U_{S''} \\ &= \begin{pmatrix} 0 & H_{A-H}^+(k) \\ H_{A-H}^-(k) & 0 \end{pmatrix}, \quad (27) \end{aligned}$$

Here  $U_{S''}$  is the unitary matrix in which  $S''$  is diagonal. Explicit form of  $U_{S''}$  and  $H_{A-H}^+(k)$  are given in the Appendix. After writing the Hamiltonian in the off-diagonal block form we calculate the winding number using Eq.11 Figure 15 illustrates the plot for the winding number for

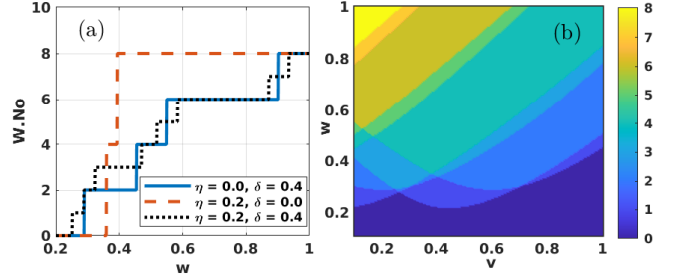


Figure 15. In panel (a) we plot winding number against  $w$  for different parameters as mentioned in the inset. The blue line shows all possible even winding number. The dashed brown line shows winding number multiple of four. The black dashed line shows all possible integer up to eight. In the panel (b), a density plot of winding number is presented in  $v - w$  plane for  $\eta = 0.2, \delta = 0.3, \gamma = 0.05, \alpha_{R1} = 0.3, \alpha_{R2} = 0.1$ . Different colored region contains all possible winding numbers up to eight which is maximally possible. Each topological phase with winding number  $W = n$  is associated with  $2n$  edge modes as expected.

four chain. Here in panel (a), we plot winding number against  $w$  for various set of parameters. The blue one depicts the plot which realizes all even winding number. On the other hand the dashed brown plot depicts winding number in multiple of four. The black dashed line depicts all possible winding number. In Fig.15 panel (b), we show contour plot of winding number in  $w - v$  plane for  $\eta = 0.2, \delta = 0.3, \gamma = 0.05, \alpha_{R1} = 0.3, \alpha_{R2} = 0.1$ . Thus we observe that the zero-energy modes can be controlled easily by manipulating the hopping parameters which could be of practical uses such as switching devices.

#### IV. EFFECT OF DOMAIN WALL

Having described the effect of various parameters in detail for extended Haldane model and also its extension to few coupled even number of chains, we now present our result on how a domain wall onsite potential profile [75] affects the mid-gap zero energy modes in the presence of various parameters. Following [75], we replace the intercell hopping  $v$  and  $w$  as site dependent parameter having distribution  $t_n = t_0(1 + (-1)^n u)$  with  $u = u_0 \tanh \left[ \frac{n-n_0}{\xi/a} \right]$ . Here the index  $n$  denotes the location of  $n$ -th site not the  $n$ -th unit cell. Thus  $n$  even denotes inter-sublattice hopping and  $n$ -odd denotes a intra-sublattice hopping for the translation invariant case.

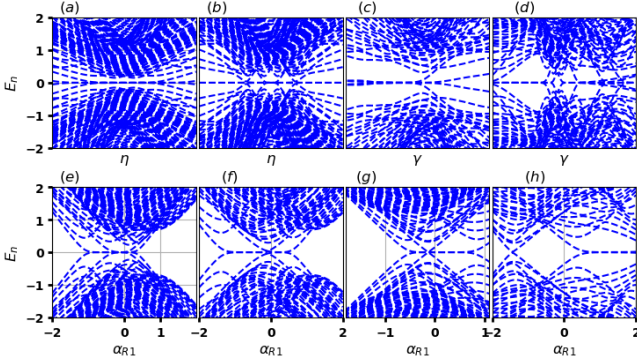


Figure 16. Energy-spectra are plotted in the absence of domain wall for various set of parameter as described while  $v = 0.2$ ,  $w = 1$ , and  $\alpha_{R2} = 0.6$  are kept fixed for all the plots. Panel (a) and (b) depict energy as a function of  $\eta$ . In (a), we consider  $\eta = \eta_1$ , with  $\gamma_2 = \eta_2 = 0$  and  $\gamma = \gamma_1 = 0.5$ . In (b),  $\eta = -\eta_2$ , with  $\gamma_1 = \eta_1 = 0$  and  $\gamma = \gamma_2 = 0.5$ . Similarly panel (c) and (d) depict energy-spectra as a function of  $\gamma$ . In panel (c), we take  $\eta = \eta_1 = 1.5$ , with  $\gamma_2 = \eta_2 = 0$  and  $\gamma = \gamma_1$ . and in panel (d),  $\eta = -\eta_2 = 1.2$ , with  $\gamma_1 = \eta_1 = 0$  and  $\gamma = \gamma_2$ . Panel (e-h) show the energy-spectra as we vary  $\alpha_{R1}$  for different set of parameter. In panel (e) and (f), we have  $\gamma = 0.5$ ,  $\gamma_1 = 0.5$ ,  $\tilde{\gamma}_2 = 0$  with imaginary hopping values  $\eta = \eta_1 = 1, 1.5$  respectively. For panel (g) and (h), higher-order hopping terms are included, namely  $\gamma_2 = 0.5$  and  $\eta_2$ . In panel (g), we consider  $\gamma = \gamma_2 = 0.5$ ,  $\gamma_1 = 0$ ,  $\eta = -\eta_2 = 1.2$ , and  $\eta_1 = 0.0$ . In panel (h),  $\gamma = \gamma_2 = \gamma_1 = 0.5$ , and  $\eta = \eta_1 = -\eta_2 = 1.5$ .

### 1. Effect of domain wall in the eigenvalue spectra:

We observe that presence of domain wall significantly modifies the eigen energy spectra as certain parameters are varied. We explore the eigenvalue of spectra for many sets of parameter and find that it significantly captures the effect of domain wall. For this reason we first present the eigenvalue spectra in the presence and absence of domain wall in Fig. 16 and Fig. 17 respectively for different representative sets of parameter. A comparison between Fig. 16, panel (a) and panel (b) shows that the low energy eigen-spectrum around zero shows significant variations as we vary  $\eta$ . The gap can be closed and re-opened as the magnitude of  $\eta$  varies from large values to small. It also shows that while in panel (a) the low energy spectrum depends linearly on  $\eta$ , it depends non-linearly on  $\eta$  for the set of parameter used in panel (b). In Fig. 16 panel (c) and (d) shows the asymmetric effect of  $\gamma$  on the eigen-spectra for positive and negative values of  $\gamma$ . In panel (e-h) (in Fig. 16 we present the effect of  $\alpha_{R1}$ ). In general when one changes the sign of  $\alpha_{R1}$ , the spectrum changes. There are multiple gap-closing and re-opening transition. We find that in Fig. 16 (e) to (h) gap closing points are connected by continuous zero energy modes for a range of  $\alpha_{R1}$  where as in panel (h), the gap-closing points are disconnected by such continuous zero energy modes.

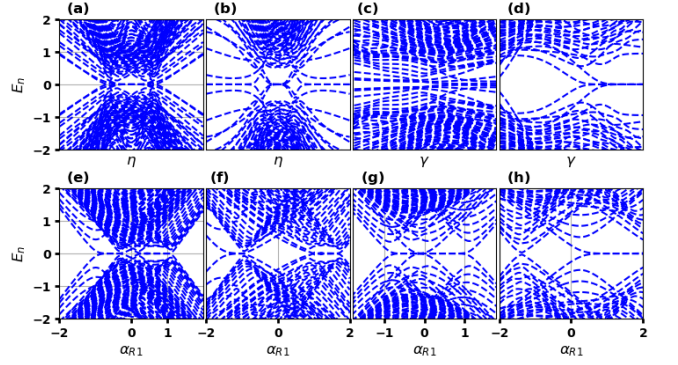


Figure 17. Energy-spectrum in the presence of domain wall. The set of parameters considered in a given panel (k) is identical to that of Fig. 16.

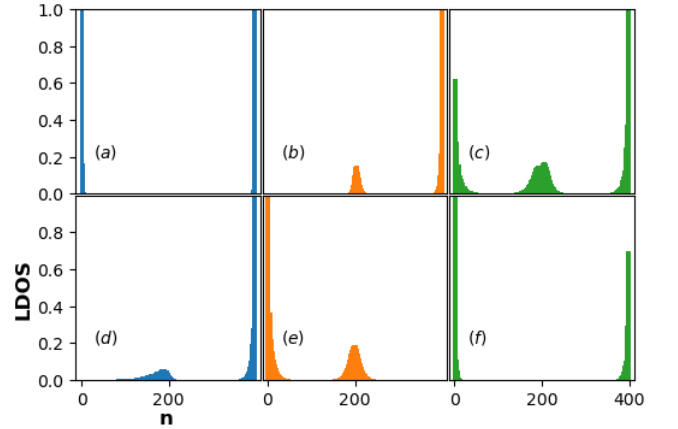


Figure 18. Linear Density of state for single chain (a) $\gamma = \gamma_1 = 0.5$ ,  $\eta = \eta_1 = 1$ , with  $\gamma_2 = \eta_2 = 0$ , (b) $\gamma = \gamma_1 = 0.5$ ,  $\eta = \eta_1 = 1.0$ , with  $\gamma_2 = \eta_2 = 0$ . (c) $\gamma = \gamma_1 = 0.5$ ,  $\eta = \eta_1 = 1.5$ , with  $\gamma_2 = \eta_2 = 0$ , (d) $\gamma = \gamma_1 = \gamma_2 = 0.5$ ,  $\eta = \eta_1 = \eta_2 = 1.5$ , (e) $\gamma = \gamma_2 = 0.5$ ,  $\eta = -\eta_2 = 1.2$ , with  $\gamma_1 = \eta_1 = 0$ . (f) $\gamma = \gamma_1 = \gamma_2 = 0.5$ ,  $\eta = \eta_1 = -\eta_2 = 1.5$ . The parameters common to all plots are  $N = 400$ ,  $n_0 = 200$ ,  $\xi = 10$ ,  $a = 1$ ,  $u_0 = 1$ ,  $\alpha_{R1} = 0.2$ , and  $\alpha_{R2} = 0.6$ .

Having described how the energy-spectrum changes by varying certain parameters in the absence of domain-wall, we now show the effect of domain-wall in energy-spectrum in Fig. 17. The parameters are chosen such that a panel (k) in Fig. 17 and 16 corresponds to same parameters in the presence and absence of domain wall respectively. A comparison of different panels in Fig. 17 and 16 shows that inclusion of domain-wall does not change the symmetric or asymmetric nature of eigenvalue spectrum with respect to certain parameters. For example in panel (a) in Fig. 16 and Fig. 17 remain symmetric in both cases. However the number of gap-closing points for the parameter ranges considered can change a lot and depending on the set of parameters it can increase or

decrease. For example in panel (d) in Fig. 16 there are more gap closing points than in panel (d) in Fig. 17. On the otherhand panel (e) in Fig. 16 has less gap-closing point than in panel (e) in Fig. 17. However in general we find that inclusion of domain wall draws more energy-eigenvalues near to zero.

## 2. Effect of domain wall on the location of zero-energy mid-gap states:

We now discuss the effect various parameters on the localization of zero energy mid gap modes. We find, by numerical experiment, that the appearances of edge modes in the presence of domain-wall can be controlled to a large extent. We briefly present our finding how it can be moved from one edge to the middle and to the other edge by varying system parameters. We first begin by describing the effect of domain wall in single chain.

### Study of single Chain

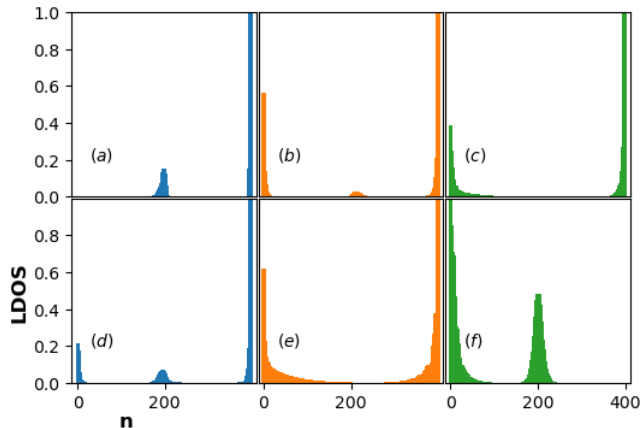


Figure 19. Zero energy edge mode in the presence of domain wall for two coupled chain are shown. For all the panels we have considered  $\delta = 2, \alpha_{R1} = 0.2, \alpha_{R2} = 0.6, u_0 = 0.1, \xi = 0, a = 1, N = 400, n_0 = 200$ . In panel (a) the parameters are  $\eta = \eta_1 = 0.1, \gamma = \gamma_1 = 0.5, \gamma_2 = \eta_2 = 0$ . For panel (b) we consider  $\eta = \eta_1 = 1, \gamma = \gamma_1 = 0.5, \gamma_2 = \eta_2 = 0$ . For panel (c)  $\eta = \eta_1 = \eta_2 = 1, \gamma = \gamma_1 = \gamma_2 = 0.5$ . Panel (d) corresponds  $\eta = \eta_1 = -\eta_2 = 1, \gamma = \gamma_1 = \gamma_2 = 0.5$ . For panel (e)  $\eta = \eta_1 = -\eta_2 = 3, \gamma = \gamma_1 = \gamma_2 = 0.5$ . For panel (f)  $\eta = -\eta_2 = 3, \gamma = \gamma_1 = \gamma_2 = 0.5, \eta_1 = 0$ .

In Fig. 18 we present the effect of domain wall for single chain. It is known that in the absence of a domain wall, edge states are localized at the ends of the lattice sites, which is shown in Fig. 18(a). When a domain wall is introduced, the edge state from one side of the lattice shifts toward the center, as depicted in 18(b). We note that in panel (b) Fig. 18 all the parameters considered in Eq. 1 are finite. In panel (c) as the parameter  $\eta$  is further increased, an additional edge state reappears at the left

end. In Fig. 18, panel (d,e,f) we present the effect of  $\tilde{\gamma}_2$  i.e a NNNNN hopping. In 18(d), the introduction of the parameter  $\tilde{\gamma}_2$  results in a shift of the zero modes, which become localized at the domain wall. Additionally, in 18(e), we reverse the polarity of  $\eta_2$ , leading to a special case where, if  $\tilde{\gamma}_1 = 0$ , the zero modes switch sides, meaning the zero mode appears at opposite side. Finally, in 18(f), with  $\tilde{\gamma}_1 \neq 0$ , we observe the reemergence of edge modes at the chain boundaries.

### Coupled chain with domain wall, $\delta \neq 0$

In Fig. 19, we have presented the effect of domain wall for coupled chain system. The parameters are specifically chosen to show how different way the domain wall can effect the location of zero energy mode. In Fig. 19 panel (a) we depict a scenario such that the zero energy mid gap state is localized in the middle and at the right side. In panel (b), we depicts a situation where the edge-modes are localized at the both-end as well in the middle also. We note that for panel (a) and (b), the value of  $\eta, \eta_1$  have increased from 0.1 to 1 while other parameters are kept fixed as written in the caption of Fig. 19. In panel (c), we have shown how the zero energy modes can be localized again at the edge by turning on  $\eta_2$  and  $\gamma_2$  to 1 and 0.5 respectively. All other parameters are identical as considered in panel (b). In panel (d), we have shown that if one changes the sign of  $\eta_2$  (keeping all other parameters same as taken in panel (c)), the zero energy edge modes re-appears at the middle. Now Fig. 19, panel (e), we have increased the magnitude of  $\eta, \eta_1, \eta_2$  to 3 in comparison to the values considered in panel (d). Finally panel (f) depicts the scenario of re-emergence of zero energy mid gap state with bulk localization by keeping  $\eta_1 = 0$  while all other parameters are same as taken in panel (e). Thus Fig. 19 presents a systematic enumeration of how in the presence of domain wall, one can manipulate the localization profile of zero energy mid gap modes.

## V. CONCLUSION

In summary, this paper investigates an extended SSH model which considers Rashba spin-orbit interaction ( $\alpha_{R1}, \alpha_{R2}$ ), a longer range NNNN hopping  $\tilde{\gamma}, \tilde{\gamma}_1$  connecting two in-equivalent sublattices preserving Chiral symmetry. This ( $\tilde{\gamma}_1$ ) yields a NNNN hopping which connects in-equivalent sublattices belonging to ' $i$ 'th and ' $i \pm 2$ 'th unit cell yielding a  $\cos 2k$  term in the spectral function. We assume all hopping interaction to be complex in general and investigated the criteria needed for existence of different topological phases. We have found that both the spin-sectors have same topological phases if  $\tilde{\gamma}$  or  $\tilde{\gamma}_1$  are purely real irrespective of  $v, w, \alpha_{R1}$  and  $\alpha_{R2}$ . Thus our extended SSH model shows a way of topological manipulation of a given spin-sector arbitrarily and winding number can vary from  $0 \rightarrow 1 \rightarrow 2$ .

We present extensive analysis of spectrum and in particular the condition of gaplessness of it. When the  $\tilde{\gamma}_1$

term is absent, the gap closing point is easily obtained. However in the presence of  $\gamma_2$ , the gap-closing points become non-trivial for the  $\cos 2k$  term brings in complexities in the system of equation. We discuss two different way to solve it. Firstly the elimination of terms yield a cubic equation which can then yield the gapless point. Additionally it can be solved by transcendental method also. Further though presence of imaginary  $\tilde{\gamma}_1$  is required to have different winding number for each spin-sector, the parametric plot of contour of  $\tilde{h}(k)$  yields distinct contour for each spin-sector always except the simple case of only  $v, w$  being non-zero. We also provide a detailed analysis of topological characterization through the behavior of contour of  $\tilde{h}(k)$  in  $h_x(k), h_y(k)$  plane.

It is pertinent to note that there has been previous studies [57, 58, 71] which explored the role of longer range hopping beyond nearest-neighbor in SSH model. The study [57] includes a second nearest-neighbor interaction which breaks the Chiral symmetry of the system. However by considering a modulated hopping and introducing an auxiliary parameter  $\theta$ , the system is mapped to an effective two dimension whose topological classification has been obtained. In study [71], a third nearest neighbor has been considered in addition to second nearest neighbour interaction. However among two possible third nearest-neighbour only of one kind (i.e equivalent to  $\gamma$  in the present study) has been considered and topological classifications are studied along the line of previous study [57]. In Ref 58, the role of all possible third nearest-neighbour has been considered and it has been shown that depending on the value of hopping strength of first and third neighbour, the winding number could be  $\pm 1$ , establishing a two fold topological phase transitions. However the present study consider a spin-full system and includes Rashba interactions and the role of the second neighbor, its effect on the spectrum and topological phase transitions has been presented in depth.

We extend our study to systems of few coupled chains. Mainly we consider two and four coupled chain and for simplicity and the interchain coupling refers to hopping between two in-equivalent sites of respective chains. For two coupled chain, this effectively yields four decoupled SSH chains each are having an effective  $v$  which are different for each SSH chains. As shown in Table I, as we increase the value of  $w$ , it can make some or all of the fermionic sector topological. This implies that the winding number of the system could be of any integer ranging from 1 to 4. The bulk boundary correspondence are shown by existence of appropriate number of zero energy

mid gap edge modes. We have extended our study to four coupled SSH chains and find that our scheme allows to obtain winding number ranging from 1 to 8. These topological phases, again, are associated with appropriate numbers of edge modes. The fact that arbitrary topological phases and associated edge modes can be obtained in simultaneous present of interchain coupling and imaginary  $\tilde{\gamma}_1$ , promises practical usage of such coupled chains in future applications. One may note that in a previous study [89] two coupled SSH chain has been studied with similar interchain coupling as considered here. The study [89] find multi-critical point as ours. Thus our study yields a natural generalization to spin-ful system and a NNNN hopping yielding much rich topological structure.

Finally we have considered the effect of domain wall in such extended SSH model as well in the two coupled chain system. Our study on the energy spectra shows that if the it is symmetric for a certain parameter changing sign in the absence of domain wall, it remains so in the presence of it. On the other hand, the presence of domain wall appears to bring more high energy bulk modes near to zero. The number of zero energy modes also changes in the presence of domain wall. The location of topological mid gap zero energy modes at the middle and edge of the chain, depends greatly on the domain wall. As parameters are tuned, additional mid gap zero energy modes appears localized at the middle and at the other end. Thus our study depicts intricate interplay of domain wall and model parameters.

There has been some progress in realizing various aspect of SSH model recently [36–41]. Bosonic version of SSH model is realized using Rydberg atom trapped in one dimensional array of optical tweezers is used [36, 41]. A mechanical set up using metallic masses connected by string [37] is proposed to observe the topological phase transitions found in 1d-SSH model. On the other hand a lattice of coupled waveguides [38]. with staggered hopping is reported to realized the edge modes similar in SSH model. Interestingly mean-chiral displacement is used as an order parameter to establish finite winding number in an extended SSH model [73]. Recently study of disorder in SSH model is proposed in simulated topoelectric circuits [90]. All of these study shows a possibility to realize the present extended SSH model in some setting. However we leave it as a future study to examine how and what are the necessary conditions to be satisfied for such practical realizations. On the other hand, possible theoretical extension incorporating non-Hermitian effect or Floquet dynamics could reveal further topological structure which we leave for future scope.

- 
- [1] F. D. M. Haldane, Nobel lecture: Topological quantum matter, *Rev. Mod. Phys.* **89**, 040502 (2017).  
 [2] K. v. Klitzing, G. Dorda, and M. Pepper, New method for high-accuracy determination of the fine-structure constant based on quantized hall resistance, *Phys. Rev. Lett.*

- 45**, 494 (1980).  
 [3] K. von Klitzing, T. Chakraborty, P. Kim, V. Madhavan, X. Dai, J. McIver, Y. Tokura, L. Savary, D. Smirnova, A. M. Rey, C. Felsner, J. Gooth, and X. Qi, 40 years of the quantum hall effect, *Nature Reviews Physics* **2**, 397

- (2020).
- [4] L. Fu and C. L. Kane, Superconducting proximity effect and majorana fermions at the surface of a topological insulator, *Phys. Rev. Lett.* **100**, 096407 (2008).
  - [5] C. L. Kane and E. J. Mele, Quantum spin hall effect in graphene, *Phys. Rev. Lett.* **95**, 226801 (2005).
  - [6] B. A. Bernevig, T. L. Hughes, and S.-C. Zhang, Quantum spin hall effect and topological phase transition in hgte quantum wells, *Science* **314**, 1757 (2006), <https://www.science.org/doi/pdf/10.1126/science.1133734>.
  - [7] X.-L. Qi and S.-C. Zhang, Topological insulators and superconductors, *Rev. Mod. Phys.* **83**, 1057 (2011).
  - [8] C. Nayak, S. H. Simon, A. Stern, M. Freedman, and S. Das Sarma, Non-abelian anyons and topological quantum computation, *Rev. Mod. Phys.* **80**, 1083 (2008).
  - [9] A. Altland and M. R. Zirnbauer, Nonstandard symmetry classes in mesoscopic normal-superconducting hybrid structures, *Phys. Rev. B* **55**, 1142 (1997).
  - [10] C.-K. Chiu, J. C. Y. Teo, A. P. Schnyder, and S. Ryu, Classification of topological quantum matter with symmetries, *Rev. Mod. Phys.* **88**, 035005 (2016).
  - [11] M. Nakahara, *Geometry, topology and physics* (CRC Press, 2018).
  - [12] J. Cayssol and J. N. Fuchs, Topological and geometrical aspects of band theory, *Journal of Physics: Materials* **4**, 034007 (2021).
  - [13] C. W. Groth, M. Wimmer, A. R. Akhmerov, J. Tworzyno, and C. W. J. Beenakker, Theory of the topological anderson insulator, *Phys. Rev. Lett.* **103**, 196805 (2009).
  - [14] J. Li, R.-L. Chu, J. K. Jain, and S.-Q. Shen, Topological anderson insulator, *Phys. Rev. Lett.* **102**, 136806 (2009).
  - [15] Y. Xing, L. Zhang, and J. Wang, Topological anderson insulator phenomena, *Phys. Rev. B* **84**, 035110 (2011).
  - [16] T. Nag and B. Roy, Anomalous and normal dislocation modes in floquet topological insulators, *Communications Physics* **4**, 157 (2021).
  - [17] S. S. Yamada, T. Li, M. Lin, C. W. Peterson, T. L. Hughes, and G. Bahl, Bound states at partial dislocation defects in multipole higher-order topological insulators, *Nature Communications* **13**, 2035 (2022).
  - [18] D. J. Salib, V. Juričić, and B. Roy, Emergent metallicity at the grain boundaries of higher-order topological insulators, *Scientific Reports* **13**, 15308 (2023).
  - [19] R. B. Laughlin, Anomalous quantum hall effect: An incompressible quantum fluid with fractionally charged excitations, *Phys. Rev. Lett.* **50**, 1395 (1983).
  - [20] S. Jana, A. Saha, and A. Mukherjee, Impact of strong correlations on a band topological insulator on the lieb lattice, *Phys. Rev. B* **100**, 045420 (2019).
  - [21] S. Jana, P. Mohan, A. Saha, and A. Mukherjee, Tailoring metal-insulator transitions and band topology via off-resonant periodic drive in an interacting triangular lattice, *Phys. Rev. B* **101**, 115428 (2020).
  - [22] S. Mandal and S. Gupta, Interacting fermions in two dimension in simultaneous presence of disorder and magnetic field, *Journal of Physics: Condensed Matter* **34**, 215602 (2022).
  - [23] F. D. M. Haldane, Model for a quantum hall effect without landau levels: Condensed-matter realization of the "parity anomaly", *Phys. Rev. Lett.* **61**, 2015 (1988).
  - [24] A. Y. Kitaev, Unpaired majorana fermions in quantum wires, *Physics-Uspekhi* **44**, 131 (2001).
  - [25] W. P. Su, J. R. Schrieffer, and A. J. Heeger, Solitons in polyacetylene, *Phys. Rev. Lett.* **42**, 1698 (1979).
  - [26] A. J. Heeger, S. Kivelson, J. R. Schrieffer, and W. P. Su, Solitons in conducting polymers, *Rev. Mod. Phys.* **60**, 781 (1988).
  - [27] G. Jotzu, M. Messer, R. Desbuquois, M. Lebrat, T. Uehlinger, D. Greif, and T. Esslinger, Experimental realization of the topological haldane model with ultracold fermions, *Nature* **515**, 237 (2014).
  - [28] S. K. Kim, H. Ochoa, R. Zarzuela, and Y. Tserkovnyak, Realization of the haldane-kane-mele model in a system of localized spins, *Phys. Rev. Lett.* **117**, 227201 (2016).
  - [29] H.-S. Kim and H.-Y. Kee, Realizing haldane model in fe-based honeycomb ferromagnetic insulators, *npj Quantum Materials* **2**, 20 (2017).
  - [30] W. Zhao, K. Kang, Y. Zhang, P. Knüppel, Z. Tao, L. Li, C. L. Tschirhart, E. Redekop, K. Watanabe, T. Taniguchi, A. F. Young, J. Shan, and K. F. Mak, Realization of the haldane chern insulator in a moiré lattice, *Nature Physics* **20**, 275 (2024).
  - [31] T. Dvir, G. Wang, N. van Loo, C.-X. Liu, G. P. Mazur, A. Bordin, S. L. D. ten Haaf, J.-Y. Wang, D. van Driel, F. Zatelli, X. Li, F. K. Malinowski, S. Gazibegovic, G. Badawy, E. P. A. M. Bakkers, M. Wimmer, and L. P. Kouwenhoven, Realization of a minimal kitaev chain in coupled quantum dots, *Nature* **614**, 445 (2023).
  - [32] B. Pandey, N. Kaushal, G. Alvarez, and E. Dagotto, Majorana zero modes in y-shape interacting kitaev wires, *npj Quantum Materials* **8**, 51 (2023).
  - [33] Y. Oreg, G. Refael, and F. von Oppen, Helical liquids and majorana bound states in quantum wires, *Phys. Rev. Lett.* **105**, 177002 (2010).
  - [34] R. M. Lutchyn, J. D. Sau, and S. Das Sarma, Majorana fermions and a topological phase transition in semiconductor-superconductor heterostructures, *Phys. Rev. Lett.* **105**, 077001 (2010).
  - [35] J. D. Sau, R. M. Lutchyn, S. Tewari, and S. Das Sarma, Generic new platform for topological quantum computation using semiconductor heterostructures, *Phys. Rev. Lett.* **104**, 040502 (2010).
  - [36] V. Lienhard, S. de Léséleuc, P. Scholl, D. Barredo, T. Lahaye, and A. Browaeys, Experimental realization of a bosonic version of the su-schrieffer-heeger (ssh) model with rydberg atoms, in *Quantum Information and Measurement (QIM) V: Quantum Technologies* (Optica Publishing Group, 2019) p. F4B.2.
  - [37] L. Thatcher, P. Fairfield, L. Merlo-Ramírez, and J. M. Merlo, Experimental observation of topological phase transitions in a mechanical 1d-ssh model, *Physica Scripta* **97**, 035702 (2022).
  - [38] G. Cáceres-Aravena, B. Real, D. Guzmán-Silva, A. Amo, L. E. F. Foa Torres, and R. A. Vicencio, Experimental observation of edge states in ssh-stub photonic lattices, *Phys. Rev. Res.* **4**, 013185 (2022).
  - [39] S. Guo, J. Huang, R. Huang, F. Zhuang, S. Su, Z. Lin, W. Qiu, J. Su, and X. Wang, Realization of higher-order topology in bilayer asymmetric Su-Schrieffer-Heeger topological electric circuits, *Applied Physics Letters* **124**, 073104 (2024), [https://pubs.aip.org/aip/apl/article-pdf/doi/10.1063/5.0191076/19673221/073104\\_1\\_5.0191076.pdf](https://pubs.aip.org/aip/apl/article-pdf/doi/10.1063/5.0191076/19673221/073104_1_5.0191076.pdf).
  - [40] M. Atala, M. Aidelsburger, J. T. Barreiro, D. Abanin, T. Kitagawa, E. Demler, and I. Bloch, Direct measurement of the zak phase in topological bloch bands, *Nature Physics* **9**, 795 (2013).
  - [41] S. de Léséleuc, V. Lienhard, P. Scholl, D. Barredo, S. Weber, N. Lang, H. P. Büchler, T. Lahaye,

- and A. Browaeys, Observation of a symmetry-protected topological phase of interacting bosons with rydberg atoms, *Science* **365**, 775 (2019), <https://www.science.org/doi/pdf/10.1126/science.aav9105>.
- [42] M. Jałochowski, M. Krawiec, and T. Kwapiński, Implementation of the su–schrieffer–heeger model in the self-assembly si–in atomic chains on the si(553)–au surface, *ACS Nano* **18**, 12861 (2024).
- [43] N. Leumer, M. Marganska, B. Muralidharan, and M. Grifoni, Exact eigenvectors and eigenvalues of the finite kitaev chain and its topological properties, *Journal of Physics: Condensed Matter* **32**, 445502 (2020).
- [44] N. Leumer, M. Marganska, B. Muralidharan, and M. Grifoni, Exact eigenvectors and eigenvalues of the finite kitaev chain and its topological properties, *Journal of Physics: Condensed Matter* **32**, 445502 (2020).
- [45] G. Li, P. Zhang, and T. Zhang, Entanglement of remote material qubits through nonexciting interaction with single photons, *Phys. Rev. A* **97**, 053808 (2018).
- [46] R. Wakatsuki, M. Ezawa, Y. Tanaka, and N. Nagaosa, Fermion fractionalization to majorana fermions in a dimerized kitaev superconductor, *Phys. Rev. B* **90**, 014505 (2014).
- [47] C. L. Kane and E. J. Mele, Quantum spin hall effect in graphene, *Phys. Rev. Lett.* **95**, 226801 (2005).
- [48] S. Saha, T. Nag, and S. Mandal, Eightfold quantum hall phases in a time reversal symmetry broken tight binding model, *Phys. Rev. B* **103**, 235154 (2021).
- [49] S. Saha, T. Nag, and S. Mandal, Multiple higher-order topological phases with even and odd pairs of zero-energy corner modes in a c3symmetry broken model, *Europhysics Letters* **142**, 56002 (2023).
- [50] S. Mondal and S. Basu, Topological features of the haldane model on a dice lattice: Flat-band effect on transport properties, *Phys. Rev. B* **107**, 035421 (2023).
- [51] S. Mondal and S. Basu, Topological phases of a semi-dirac chern insulator in the presence of extended range hopping, *Phys. Rev. B* **105**, 235441 (2022).
- [52] S. Mondal and S. Basu, Vanishing of the quantum spin hall phase in a semi-dirac kane-mele model, *Phys. Rev. B* **105**, 235409 (2022).
- [53] A. Mukherjee, A. Nandy, S. Sil, and A. Chakrabarti, Tailoring flat bands and topological phases in a multistrand creutz network, *Phys. Rev. B* **105**, 035428 (2022).
- [54] C. Li, S. Lin, G. Zhang, and Z. Song, Topological nodal points in two coupled su–schrieffer–heeger chains, *Phys. Rev. B* **96**, 125418 (2017).
- [55] A. Sivan and M. Orenstein, Topology of multiple cross-linked su–schrieffer–heeger chains, *Phys. Rev. A* **106**, 022216 (2022).
- [56] S.-L. Zhang and Q. Zhou, Two-leg su–schrieffer–heeger chain with glide reflection symmetry, *Phys. Rev. A* **95**, 061601 (2017).
- [57] L. Li, Z. Xu, and S. Chen, Topological phases of generalized su–schrieffer–heeger models, *Phys. Rev. B* **89**, 085111 (2014).
- [58] Y. Betancur-Ocampo, B. Manjarrez-Montañez, A. M. Martínez-Argüello, and R. A. Méndez-Sánchez, Twofold topological phase transitions induced by third-nearest-neighbor hoppings in one-dimensional chains, *Phys. Rev. B* **109**, 104111 (2024).
- [59] M. Z. Hasan and C. L. Kane, Colloquium: Topological insulators, *Rev. Mod. Phys.* **82**, 3045 (2010).
- [60] Y. Hou, T. Zhang, J. Sun, L. Liu, Y. Yao, and Y. Wang, Progress on 2d topological insulators and potential applications in electronic devices\*, *Chinese Physics B* **29**, 097304 (2020).
- [61] W. Tian, W. Yu, J. Shi, and Y. Wang, The property, preparation and application of topological insulators: A review, *Materials* **10**, 10.3390/ma10070814 (2017).
- [62] M. J. Gilbert, Topological electronics, *Commun Phys* **4**, 70 (2021).
- [63] S. Mondal and S. Basu, Band-engineered bilayer haldane model: Evidence of multiple topological phase transitions, *Phys. Rev. B* **108**, 045307 (2023).
- [64] X. Wu, C. X. Zhang, and M. A. Zubkov, Multilayer haldane model, *Solid State Communications* **353**, 114863 (2022), eprint: arXiv:2101.01068.
- [65] B. Ostahie and A. Aldea, Stacking model of a three-dimensional second-order topological insulator manifesting quantum anomalous hall effect, *Phys. Rev. Res.* **6**, 023168 (2024).
- [66] F. Liu and K. Wakabayashi, Novel topological phase with a zero berry curvature, *Phys. Rev. Lett.* **118**, 076803 (2017).
- [67] A. Agrawal and J. N. Bandyopadhyay, Cataloging topological phases of  $n$  stacked su–schrieffer–heeger chains by a systematic breaking of symmetries, *Phys. Rev. B* **108**, 104101 (2023).
- [68] J. Kim, C.-Y. Huang, H. Lin, D. Vanderbilt, and N. Kioussis, Bismuth antiphase domain wall: A three-dimensional manifestation of the su–schrieffer–heeger model, *Phys. Rev. B* **107**, 045135 (2023).
- [69] F. Liu, Analytic solution of the  $n$ -dimensional su–schrieffer–heeger model, *Phys. Rev. B* **108**, 245140 (2023).
- [70] S. Verma and T. K. Ghosh, Bulk-boundary correspondence in extended trimer su–schrieffer–heeger model, *Phys. Rev. B* **110**, 125424 (2024).
- [71] C.-F. Li, X.-P. Li, and L.-C. Wang, Topological phases of modulated su–schrieffer–heeger chains with long-range interactions, *Europhysics Letters* **124**, 37003 (2018).
- [72] A. Agrawal and J. N. Bandyopadhyay, Floquet topological phases with high chern numbers in a periodically driven extended su–schrieffer–heeger model, *Journal of Physics: Condensed Matter* **34**, 305401 (2022).
- [73] D. Xie, W. Gou, T. Xiao, and et al., Topological characterizations of an extended su–schrieffer–heeger model, *npj Quantum Inf* **5**, 55 (2019).
- [74] S. Mandal and S. Kar, Topological solitons in a su–schrieffer–heeger chain with periodic hopping modulation, domain wall, and disorder, *Phys. Rev. B* **109**, 195124 (2024).
- [75] M. Scollon and M. P. Kennett, Persistence of chirality in the su–schrieffer–heeger model in the presence of on-site disorder, *Phys. Rev. B* **101**, 144204 (2020).
- [76] R. Dias and A. Marques, Long-range hopping and indexing assumption in one-dimensional topological insulators, *Physical Review B* **105**, 035102 (2022).
- [77] P. Kokhanchik, D. Solnyshkov, T. Stöferle, B. Piętko, J. Szczytko, and G. Malpuech, Modulated rashba-dresselhaus spin-orbit coupling for topology control and analog simulations, *Physical Review Letters* **129**, 246801 (2022).
- [78] N. Ahmadi, J. Abouie, and D. Baeriswyl, Topological and nontopological features of generalized su–schrieffer–heeger models, *Physical Review B* **101**, 195117 (2020).



- [79] X. Zhou, J.-S. Pan, and S. Jia, Exploring interacting topological insulator in the extended su-schrieffer-heeger model, *Physical Review B* **107**, 054105 (2023).
- [80] J. Zurita, C. E. Creffield, and G. Platero, Topology and interactions in the photonic creutz and creutz-hubbard ladders, *Advanced Quantum Technologies* **3**, 1900105 (2020), <https://onlinelibrary.wiley.com/doi/pdf/10.1002/qute.201900105>.
- [81] M. Jangjan and M. V. Hosseini, Topological properties of subsystem-symmetry-protected edge states in an extended quasi-one-dimensional dimerized lattice, *Phys. Rev. B* **106**, 205111 (2022).
- [82] M. Jangjan and M. V. Hosseini, Floquet engineering of topological metal states and hybridization of edge states with bulk states in dimerized two-leg ladders, *Sci Rep* **10**, 14256 (2020).
- [83] B. Hetényi and M. Yahyavi, Topological insulation in a ladder model with particle-hole and reflection symmetries, *Journal of Physics: Condensed Matter* **30**, 10LT01 (2018).
- [84] K. Monkman and J. Sirker, Operational entanglement of symmetry-protected topological edge states, *Phys. Rev. Res.* **2**, 043191 (2020).
- [85] C. Borja, E. Gutiérrez, and A. López, Emergence of floquet edge states in the coupled su-schrieffer-heeger model, *Journal of Physics: Condensed Matter* **34**, 205701 (2022).
- [86] S. Ryu, A. P. Schnyder, A. Furusaki, and A. W. Ludwig, Topological insulators and superconductors: tenfold way and dimensional hierarchy, *New Journal of Physics* **12**, 065010 (2010).
- [87] C.-K. Chiu, J. C. Teo, A. P. Schnyder, and S. Ryu, Classification of topological quantum matter with symmetries, *Reviews of Modern Physics* **88**, 035005 (2016).
- [88] D. Mondal, A. K. Ghosh, T. Nag, and A. Saha, Topological characterization and stability of floquet majorana modes in rashba nanowires, *Physical Review B* **107**, 035427 (2023).
- [89] C. Li, S. Lin, G. Zhang, and Z. Song, Topological nodal points in two coupled su-schrieffer-heeger chains, *Phys. Rev. B* **96**, 125418 (2017).
- [90] J. C. Pérez-Pedraza, J. E. Barrios-Vargas, and A. Raya, Impact of impurities on the topological boundaries and edge state localization in a staggered chain of atoms: Ssh model and its topoelectrical circuit realization (2024), arXiv:2402.05261 [cond-mat.mtrl-sci].

## Appendix

### Appendix A: Gap closing condition in the presence of $\cos 2k$ term

Here we briefly outline how to obtain the value of ‘ $k$ ’ which corresponds to gap-closing point during topological phase transition. For this we rewrite Eqs. 12,13,14,15 for reference purposes.

$$h_{\uparrow,x}^k = v + (w + \gamma) \cos k + (\eta - \alpha_{R2}) \sin k + \gamma_1 \cos 2k - \frac{\eta_1}{2} \sin 2k \quad (\text{A1})$$

$$h_{\uparrow,y}^k = \alpha_{R1} + (w - \gamma) \sin k + \alpha_{R2} + \gamma_1 \sin 2k + \frac{\eta_1}{2} \cos 2k \quad (\text{A2})$$

$$h_{\downarrow,x}^k = v + (w + \gamma) \cos k + (\alpha_{R2} + \eta) \sin k + \gamma_1 \cos 2k - \frac{\eta_1}{2} \sin 2k \quad (\text{A3})$$

$$h_{\downarrow,y}^k = -\alpha_{R1} - \alpha_{R2} \cos k + (w - \gamma) \sin k + \gamma_1 \sin 2k + \frac{\eta_1}{2} \cos 2k \quad (\text{A4})$$

We note that  $h_{\uparrow,y}^k = 0$  yields the condition for  $\sin k$  as below (with the substitution  $\sin 2k = 2 \cos k \sin k$ ),

$$\sin k = \frac{\alpha_{R1} - \alpha_{R2} - \eta \cos 2k}{w - \gamma + 2\gamma \cos k} \quad (\text{A5})$$

The above equation yields certain conditions such that  $|\sin k| \leq 1$ . The Eqn. A5 also suggests that  $w - \gamma + 2\gamma \cos k \neq 0$ . Provided these conditions are satisfied one can substitute for  $\sin k$  in Eqn. A1 and uses  $\cos 2k = 1 - 2\cos^2 k$ , one obtains a cubic equation for  $\cos k$ . The

cubic equation obtained with  $x = \cos k$  is given below.

$$a \cdot x^3 + b \cdot x^2 + c \cdot x + d = 0 \quad (\text{A6})$$

where the coefficients are defined as (with  $\alpha_{Ri} = \alpha_i$ ):

$$a = \eta^2 + 4\gamma^2, \quad (\text{A7})$$

$$b = 2\alpha_2\eta + \eta^2 + 4\gamma w, \quad (\text{A8})$$

$$c = \alpha_2(\alpha_2 + \eta) - \alpha_1\eta - \frac{1}{2}\eta^2 - 3\gamma^2 + 2\gamma v + w^2, \quad (\text{A9})$$

$$d = -\alpha_1(\alpha_2 + \eta) - \frac{\eta}{2}(\alpha_2 + \eta) + \gamma(\gamma - v - w) + vw. \quad (\text{A10})$$

The solutions for  $x$  are given by:

$$x_1 = -\frac{b}{3a} - \frac{2^{1/3}(-b^2 + 3ac)}{3a \left( -2b^3 + 9abc - 27a^2d + \sqrt{-4(b^2 - 3ac)^3 + (2b^3 - 9abc + 27a^2d)^2} \right)^{1/3}} + \frac{\left( -2b^3 + 9abc - 27a^2d + \sqrt{-4(b^2 - 3ac)^3 + (2b^3 - 9abc + 27a^2d)^2} \right)^{1/3}}{3 \cdot 2^{1/3}a}, \quad (\text{A11})$$

$$x_2 = -\frac{b}{3a} + \frac{(1 + i\sqrt{3})(-b^2 + 3ac)}{3 \cdot 2^{2/3}a \left( -2b^3 + 9abc - 27a^2d + \sqrt{-4(b^2 - 3ac)^3 + (2b^3 - 9abc + 27a^2d)^2} \right)^{1/3}} - \frac{(1 - i\sqrt{3}) \left( -2b^3 + 9abc - 27a^2d + \sqrt{-4(b^2 - 3ac)^3 + (2b^3 - 9abc + 27a^2d)^2} \right)^{1/3}}{6 \cdot 2^{1/3}a}, \quad (\text{A12})$$

$$x_3 = -\frac{b}{3a} + \frac{(1 - i\sqrt{3})(-b^2 + 3ac)}{3 \cdot 2^{2/3}a \left( -2b^3 + 9abc - 27a^2d + \sqrt{-4(b^2 - 3ac)^3 + (2b^3 - 9abc + 27a^2d)^2} \right)^{1/3}} - \frac{(1 + i\sqrt{3}) \left( -2b^3 + 9abc - 27a^2d + \sqrt{-4(b^2 - 3ac)^3 + (2b^3 - 9abc + 27a^2d)^2} \right)^{1/3}}{6 \cdot 2^{1/3}a} \quad (\text{A13})$$

In the present case only the real value of the root provided by  $x_1$  is used for analysis. In the below we provide the expression for  $H_{AB}^-$  and  $U_S$  used in Eq.23,

$$H_{AB}^- = \begin{pmatrix} j_1(k) & 0 & \delta & 0 \\ 0 & j_2(k) & 0 & \delta \\ \delta & 0 & j_1(k) & 0 \\ 0 & \delta & 0 & j_2(k) \end{pmatrix} \quad (\text{A14})$$

$$U_S = \begin{pmatrix} 0 & 0 & 0 & 0 & 0 & 0 & 0 & 1 \\ 0 & 0 & 0 & 0 & 0 & 0 & 1 & 0 \\ 0 & 0 & 1 & 0 & 0 & 0 & 0 & 0 \\ 0 & 1 & 0 & 0 & 0 & 0 & 0 & 0 \\ 0 & 0 & 0 & 0 & 0 & 1 & 0 & 0 \\ 0 & 0 & 0 & 0 & 1 & 0 & 0 & 0 \\ 0 & 1 & 0 & 0 & 0 & 0 & 0 & 0 \\ 1 & 0 & 0 & 0 & 0 & 0 & 0 & 0 \end{pmatrix}, \quad (\text{A15})$$

The expressions for  $j_1(k)$  and  $j_2(k)$  are given below.

$$j_1(k) = v - i\alpha_1 + e^{ik} \left( w + i \left( \alpha_2 + \frac{\xi}{2} \right) \right) + e^{-ik} \left( i\frac{\eta}{2} + \gamma \right) + e^{2ik} \left( i\frac{\eta_1}{2} + \gamma_1 \right) \quad (\text{A16})$$

$$j_2(k) = v + i\alpha_1 + e^{ik} \left( w - i \left( \alpha_2 - \frac{\xi}{2} \right) \right) + e^{-ik} \left( i\frac{\eta}{2} + \gamma \right) + e^{2ik} \left( i\frac{\eta_1}{2} + \gamma_1 \right) \quad (\text{A17})$$

Finally the expressions for  $H_{AH}^-$  and  $U_S''$  used in Eq. 27 are as follows,

$$H_{AH}^- = \begin{pmatrix} j_2(k) & 0 & \delta & 0 & 0 & 0 & 0 & 0 \\ 0 & j_1(k) & 0 & \delta & 0 & 0 & 0 & 0 \\ \delta & 0 & j_2(k) & 0 & \delta & 0 & 0 & 0 \\ 0 & \delta & 0 & j_1(k) & 0 & \delta & 0 & 0 \\ 0 & 0 & \delta & 0 & j_2(k) & 0 & \delta & 0 \\ 0 & 0 & 0 & \delta & 0 & j_1(k) & 0 & \delta \\ 0 & 0 & 0 & 0 & \delta & 0 & j_2(k) & 0 \\ 0 & 0 & 0 & 0 & 0 & \delta & 0 & j_1(k) \end{pmatrix} \quad (\text{A18})$$

